Radiosynthesis and biological evaluation of [^{68}Ga]Ga-NOTA-Folate in experimental atherosclerosis and myocardial infarction models.

Erika del Carmen Atencio Herre

Turun yliopisto
University of Turku

Master's Thesis

University of Turku
11.05.2020

Master's Degree of Biomedical Imaging
PET Imaging

Credits: 20 ECTS

Supervisors:
1: Anne Roivainen

2: Xiang-Guo Li

3: Antti Saraste

4: Riku Klén

Passed:

Grade

The originality of this thesis has been checked in accordance with the University of Turku quality assurance system using the Turnitin Originality Check service.

Abstract

Univeristy of Turku
Faculty of Medicine, Institute of Biomedicine
Turku PET Centre

Erika del Carmen Atencio Herre:

Radiosynthesis and biological evaluation of [^{68}Ga]Ga-NOTA-Folate in experimental atherosclerosis and myocardial infarction models.

Master's thesis, 62 pp.
PET Imaging
May 2020

While many folate-receptor (FR) targeting radiotracers have been studied for imaging cancers, there is a need for tracers that target inflammation for diagnostic and monitoring purposes. Two diseases in which inflammation plays a key role are atherosclerosis and myocardial infarction (MI). Inflammation is critical to the development and progression of atherosclerosis, which can lead to MI. Higher macrophage levels have been associated with adverse remodeling effects in post-MI healing. Given the commonality of these potentially fatal conditions, it is of great interest to have a reliable radiotracer available for non-invasive detection and monitoring. As FR-β expression is upregulated in active macrophages, it serves as a great target for imaging of inflammation. [^{68}Ga]Ga-NOTA-Folate, a new FR-targeting radiotracer, was synthesized and biologically evaluated to assess its ability to target inflammation in mouse and human atherosclerotic lesions. Mice were studied using *in vivo* positron emission tomography and *ex vivo* digital autoradiography of aorta sections. Human carotid artery tissues were studied *in vitro* for tracer binding. In addition, rat heart tissue sections were incubated *in vitro* with [^{68}Ga]Ga-NOTA-Folate to evaluate post-MI healing. Upon analyzing the *in vitro* binding, [^{68}Ga]Ga-NOTA-Folate showed significantly higher binding in atherosclerotic lesions when compared to tissues treated with folate glucosamine, a FR blocker, indicating specificity of [^{68}Ga]Ga-NOTA-Folate via FRs. As the atherosclerotic lesions observed in the experimental mice were not so extensive, more *in vivo* studies should be done to verify the results.

KEYWORDS: Positron emission tomography; Inflammation; Atherosclerosis; Myocardial Infarction, [^{68}Ga]Ga-NOTA-Folate.

ABBREVIATIONS

[^{18}F]FDG	2-Deoxy-2-[^{18}F]-fluoro-*D*-glucose
^{18}F	Fluorine-18
^{68}Ga	Gallium-68
^{68}Ga-DOTATATE	^{68}Ga-[1,4,7,10-tetraazacyclododecane-1,4,7,10-tetraacetic acid]-(Tyr^3)-octreotate
A_m	Molar activity
ACE	Angiotensin-converting enzyme
ApoB100	Apolipoprotein B100
ARG	Autoradiography
CHD	Coronary heart disease
CPS	Counts per second
CT	Computed tomography
CVD	Cardiovascular disease
DOTA	1,4,7,10-Tetraazacyclododecane-1,4,7,10-tetraacetic acid
EP-H_2O	Extra-pure Milli-Q water (182 Ω)
FR	Folate receptor
FR+	Folate receptor positive
FR-α	Folate receptor alpha
FR-β	Folate receptor beta
Gy	Gray
H&E	Hematoxylin and eosin
HDL	High-density lipoprotein
HEPES	4-(2-Hydroxyethyl)-1-piperazineethanesulfonic acid
HPLC	High-performance liquid chromatography
iTLC	Instant thin-layer chromatography
LDL	Low-density lipoproteins
LDLR	Low-density lipoprotein receptor
MI	Myocardial infarction
MR	Magnetic resonance
NOTA	1,4,7-Triazacyclononane-*1-4-7*-triacetic acid

PBS	Phosphate-buffered saline
PET	Positron emission tomography
PSL	Photostimulated luminescence
QC	Quality control
RG	Arginine-glycine-aspartic acid peptide
ROI	Region of interest
RT	Room temperature
SCX	Strong cation exchange
SPECT	Single-photon emission computed tomography
Sv	Sievert
VLDL	Very low density lipoprotein

CONTENTS

1 INTRODUCTION

The heartbeat is the first sound of human life. The heart is the first organ we are taught how to draw when we are young, albeit not anatomically correct. Among the most fatal diseases in developed countries, coronary heart disease (CHD) is consistently the leading cause of death, accounting for as much as 23% of all deaths in the United States in 2017 (Murray, Phil, and Lopez, 2013; Kochanek et al., 2019). Given the prevalence of these diseases, and the vitalness of the integrity of our body's most precious organ, the need for a less invasive and early diagnostic means of monitoring the development or progression of CHD is paramount.

Molecular imaging is defined as "the visualization, characterization, and measurement of biological processes at the molecular and cellular levels in humans and other living systems" (Mankoff, 2007). Using noninvasive molecular imaging allows for a better understanding of diseases at the biological level, an understanding that can be used for early detection of diseases as well as disease and treatment monitoring. Radiotracers are molecules that contain a radionuclide. When used in conjunction with positron emission tomography (PET) imaging, radiotracers are used as one of several methods for molecular imaging.

As folate receptors are selectively expressed in active macrophages, [^{68}Ga]Ga-NOTA-Folate is explored as a new folate receptor-targeting radiotracer aimed at imaging inflammation present in two conditions of CHD: atherosclerosis and myocardial infarction (MI). By using *in vivo* PET/CT imaging and *ex vivo* and *in vitro* digital autoradiography, [^{68}Ga]Ga-NOTA-Folate is biologically assessed in atherosclerosis and MI experimental models.

2 REVIEW OF THE LITERATURE

2.1 Atherosclerosis

Since the 1970s, the rate of CHD deaths has seemingly decreased in most developed countries such as Japan, the USA, and around western Europe (Levi et al., 2002). As Ford et al. have detailed, 44% of the decreases in the USA are due to recognition and interventions for reducing risk factors. Such risk factors include smoking, poor dietary choices, physical inactivity and high body mass index, cholesterol levels, systolic blood pressure and fasting plasma glucose levels (Ford et al., 2007). Additionally, around 47% of the decreases in CHD deaths are due to medical treatments, such as acute MI or unstable angina treatments, preventative therapies after an initial MI, and treatments for chronic angina (Virani et al., 2020; Ford et al., 2007).

Despite CHD deaths having steadily decreased, age-adjusted rates of death have shown part of the decline is due to these deaths occurring later in life and therefore impact the overall life expectancy of various countries (Roger, 2007). Furthermore, CHD remains the leading cause of death in developed countries, accounting for just under a quarter of all 2017 deaths in the USA (Murray, Phil, and Lopez, 2013; Kochanek et al., 2019).

Atherosclerosis is a highly prevalent cardiovascular disease characterized by plaque buildup on artery walls, with disease progression relying on inflammation. Atherosclerosis is the gradual disease that begins CHD and often leads to more serious complications, such as angina, MI or death.

2.1.1 Disease Progression

Low-density lipoproteins (LDL) normally transport cholesterol and fatty acids to tissues around the body. When there is too much LDL in the blood, however, it can oxidize in the bloodstream, signaling for leukocytes and macrophages, causing inflammation and eventual

formation of foam cells, which over time turn to atherosclerotic plaques that can undergo fibrosis and calcify (Lu and Daugherty, 2015; Bentzon et al., 2014). This cascade of events narrows the artery over time, leading to CHD.

As large amounts of plaque accumulate in the arterial walls, the plaques can rupture or break off, creating a clot downstream and stopping blood flow. When a clot restricting blood flow occurs in the brain, the patient suffers from a stroke and when it occurs in one of the coronary arteries leading to the heart, the patient suffers a myocardial infarction (MI), or heart attack (Bentzon et al., 2014).

2.1.2 Risk Factors

While many CHD-related deaths occur later in life, development of atherosclerosis can occur at any time, as fatty streaks, the first stage of atherosclerosis formation, have been identified in fetal arteries (Napoli et al., 1997). Risk factors can increase the potential for atherosclerotic development. Rafieinan-Kopaei et al. have detailed several of the known risk factors of atherosclerosis, including high blood cholesterol, smoking, high blood pressure, obesity, insulin resistance, diabetes, family history, age, and inflammation (Rafieian-Kopaei et al., 2014). Having more than one of these factors further increases the chances of atherosclerotic plaque development.

Having high cholesterol, particularly LDL cholesterol, increases the chance of oxidation of LDL in the bloodstream, which triggers the atherosclerosis development cascade. In addition to restricting oxygen to the body, smoking damages blood vessels. Damage to blood vessels also occurs with high blood pressure, a condition that has been shown to speed up the development of atherosclerosis. When blood vessels are damaged, the body sends signals for repair, which causes inflammation, again triggering the cascade (Rafieian-Kopaei et al., 2014).

In addition to these risk factors, other lifestyle habits that can increase the risk of developing atherosclerosis includes having a poor diet and lack of physical activity. These habits can

worsen many of the other risk factors, such as high blood cholesterol and obesity (Rafieian-Kopaei et al., 2014). By eating foods high in cholesterol and saturated and trans fats, the risk of developing high LDL cholesterol increases. Additionally, consuming foods high in sodium can worsen high blood pressure. Changing dietary habits by reducing the consumption of these unhealthy foods and having a balanced diet with adequate plant sterol consumption can lower LDL cholesterol and raise high-density lipoprotein (HDL) cholesterol, reducing the risk of atherosclerosis (Clifton and Keogh, 2018). Furthermore, regular physical activity has been proven to positively affect the endothelial function of blood vessels as well as lipid metabolism, raising HDL cholesterol levels while lowering triglyceride levels (Al-Mamari, 2009).

2.1.3 Diagnostic Methods

While reducing manageable risk factors is a great preventative measure and treatment for the beginning stages of atherosclerosis, usually the disease has progressed too far at the point of diagnosis. Given that atherosclerosis is usually sub-clinical until angina or MI occurs, there is a need for more non-invasive diagnostic techniques to detect the disease before it progresses further. Current diagnostic methods include biomarker detection, of which high-sensitivity C-reactive protein and lipoprotein-associated phospholipase A2 serve to give prognosis of atherosclerosis by detecting risk factors such as inflammation, at which point the disease is already advanced (Shah, 2010). Additionally, there are noninvasive imaging techniques using computed tomography (CT), ultrasonography, and PET for diagnosing atherosclerosis.

CT angiography helps visualize arteries, with contrast agents aiding the visualization. Depending on the pixel density shown from the scan, plaque and calcifications can be distinguished from arterial lumen (Achenbach et al., 2004). After attenuation, plaques are seen as darker areas while calcifications are seen as brighter areas. While this provides clear images of plaques within arterial walls, the radiation exposure from the procedure makes it so that usually only patients having exhibited symptoms of atherosclerosis use this method for disease monitoring (Ibañez, Badimon, and Garcia, 2009).

Coronary calcium detection uses CT to image the cardiac region. The image is taken between heartbeats and calcification present is shown as a defined area in the image with hyper-attenuation and can be quantified using several methods, one of the most common being the Agatston method (Neves, Andrade, and Monção, 2017). Once quantified, a coronary artery calcium score is determined, which has been shown to be prognostic of cardiovascular incidence risk. Various studies have determined that a coronary artery calcium score of zero in patients with no symptoms is associated with low mortality risk in the long run, while some have also suggested that an increase in the score may be related to higher risk of a cardiovascular event (Neves, Andrade, and Monção, 2017). The latter requires further investigation to determine the true clinical value of changing scores. When used in symptomatic patients for disease monitoring, a score above zero was associated with significant stenosis observed via angiography (Neves, Andrade, and Monção, 2017).

Noninvasive ultrasonography of carotid arteries is also used for detection of atherosclerosis. As detailed by de Groot et al., doppler ultrasonography is useful in noninvasively detecting stenosis after almost half of the artery area has been compromised. Brightness ultrasonography is a newer method that measures the thickness of the carotid artery wall and plaque, known as the intima-media thickness, noninvasively. It has been determined that having over a certain amount of thickness seen in the patient's demographic group was associated with future cardiovascular events, such as MI or death, therefore having the potential of monitoring risk of a cardiovascular event (de Groot et al., 2008). As ultrasound waves cannot penetrate too deeply, noninvasive imaging is limited to vessels close to the skin's surface (Ibañez, Badimon, and Garcia, 2009).

Another noninvasive technique of growing interest for imaging atherosclerosis uses PET imaging. The advantage of PET imaging is that it shows metabolic activity rather than just anatomy, a feature that can be of great use when diagnosing and monitoring atherosclerosis. As the field is growing, only a few radiotracers are available for targeting atherosclerotic plaques, therefore there is a need for radiotracer development to both metabolically and anatomically visualize atherosclerosis.

2.1.4 Treatment

The need for treatment to manage atherosclerosis is paramount, as having the disease go unchecked can be fatal. While preventative measures through a healthy lifestyle are ideal, there are options available for treating the disease once it has progressed, most of which are targeted at managing the risk factors.

As Bergheanu, Bodde, and Jukema describe, statins are the leading drug for treating atherosclerosis. Statins are reductase inhibitors that increase expression of LDL receptors (LDLR), which take up LDL from the bloodstream. By decreasing LDL, this cam help reduce LDL oxidation in the bloodstream, preventing more plaque formation. Cholesterol absorption inhibitors also reduce LDL in the blood, as do bile acid sequestrants. To improve blood lipid levels, statins also lower blood triglycerides. Research is also ongoing to determine whether omega-3 fatty acids can also reduce blood triglyceride levels. Furthermore, HDL can be increased using statins and cholesterol ester transfer protein inhibitors (Bergheanu, Bodde, and Jukema, 2017).

As the main goal is to avoid a more serious cardiac event caused by atherosclerosis, research is being conducted for disease detection and treatment monitoring. To study the disease, an experimental mouse model deficient in low-density lipoprotein receptors and only expressing apolipoprotein B100 ($LDLR^{-/-}/ApoB^{100/100}$) can be used. By lacking LDLRs, LDL is not taken up and therefore leads to high LDL cholesterol levels. Apolipoprotein B100 (ApoB100) is part of LDL and plays a key role in the development of very low density lipoproteins (VLDL), thereby regulating lipid metabolism. When studied in mice, the combination of LDLR deficiency and the expression of apolipoprotein B100 had high cholesterol levels and were noted to have advanced atherosclerotic plaques when fed on low-fat diets (Véniant, M. M., 1998). By using this strain fed a high-fat diet, the chances of developing atherosclerotic plaques is high and serves as a good experimental atherosclerotic model.

2.2 Myocardial Infarction

A serious complication of CHD, MI is most universally defined as prolonged ischemia, or lack of oxygen, causing myocyte damage and death. This can be the result of a blood clot in a coronary artery of the heart, due to either narrowing of the artery or plaque breakoff, as well as an imbalance in oxygen supply and demand, sudden cardiac death, as well as during surgical intervention (Thygesen et al., 2007).

2.2.1 Disease Progression

When an artery is blocked, blood flow to the heart is cut off and causes an inhibition of nutrients and oxygen to the tissue downstream, known as ischemia, which leads to tissue damage. This damage varies depending on the size and location of the clot, though it causes myocyte death and a degree of necrosis nonetheless (Curley et al., 2018).

The body immediately signals for an inflammatory response to occur at the site following the tissue damage. The inflammation helps repair the tissue immediately after MI, though it leads to the eventual development of scar tissue and adverse structural and functional changes in the heart. A few of these changes seen include remodeling of the left ventricle to alter its shape and function, which can lead to a reduction of contractibility that can most likely cause eventual heart failure and death (van der Laan, Nahrendorf, and Piek, 2012).

Macrophages help during various stages of inflammation post-MI. They help in digesting the dead cells and any debris around as well as secrete growth factors to promote angiogenesis. When thinking of prognosis after MI, macrophage concentration has been shown to be a predictor of adverse remodeling effects, with increased adverse effects in function seemingly associated with higher concentrations of classical macrophages in the blood (van der Laan, Nahrendorf, and Piek, 2012). For this reason, it is of great interest to study a target-specific tracer to accurately and non-invasively image the post-MI inflammatory state, as it can help with specified treatment to lower the risk of heart failure and death.

2.2.2 Risk Factors

As atherosclerosis is part of the prerequisite of MI, the risk factors associated with development of atherosclerosis are the same as for MI, including smoking, diabetes, unhealthy blood lipid levels, and hypertension (Rafieian-Kopaei et al., 2014). Acute MI may occur for various reasons, however among many cases there are several common triggers, such as stressful events, coffee or alcohol consumption, physical exertion and heavy meals (Baccarelli and Benjamin, 2013).

2.2.3 Diagnostic Methods

There are several methods for diagnosing MI. Many biomarkers are used for the detection of myocardial damage after MI, such as creatine kinase and troponins (Howard-Alpe, Sear and Foex, 2006). There are also several imaging techniques used for visualizing MI and its healing by using magnetic resonance (MR), PET, CT and single-photon emission computed tomography (SPECT). These imaging modalities help visualize the heart's structure and function after MI (Naresh et al., 2012).

Chest X-rays are the most used tool for visualizing any ventricular disfunctions after MI (Esmaeilzadeh, Parsaee, and Maleki, 2013; Minicucci et al., 2011). Echocardiograms are done using ultrasonography to visualize cardiac function. This can help provide information regarding ventricular systolic and diastolic function, which can help diagnose MI (Esmaeilzadeh, Parsaee, and Maleki, 2013).

Using various protocols, MR has been used for MI visualization. Depending on the sequence done, information such as the morphology of the heart, presence of edema, and regional function can be given. This is then useful in determining the severity of the MI, its age, complications associated and predicting therapy responses (Rajiah et al., 2013). The images produced from MR are of great value and show great contrast, all without radiation exposure. While not as popular as MR, MI has also been diagnosed using CT scans, including the use of CT angiography (La Grutta et al., 2017, Warraich et al., 2014).

Myocardial perfusion imaging using PET can be used to visualize the blood flow of the heart after MI. For this, $[^{15}O]H_2O$, $[^{82}Rb]RbCl$, and $[^{13}N]NH_3$ are used clinically, with other radiotracers being investigated for this purpose (Li et al., 2014). Myocardial metabolism can also be imaged using PET in order to see the viability of the myocardium post MI and determine eligibility for potential revascularization surgery. The oxygen consumption of the heart may be assessed using $[^{15}O]O_2$, while oxygen metabolism may be assessed using $[^{11}C]$acetate (Li et al., 2014). A few other pre-clinical radiotracers have been designed to target MI healing; they are detailed in the *Radiotracers* section.

2.2.4 Treatment

As is the case with atherosclerosis, ideal treatment of MI would be preventative measures with a healthy lifestyle to reduce risk factors before MI occurs. This, however, is not the reality in most cases and therefore several treatment options are available following MI.

Both immediate and chronic treatments following MI can help reduce the adverse remodeling effects to prevent heart failure. As described by Minicucci et al., following MI, diuretics can be used to manage excess water and sodium present while also potentially serving as vasodilators. Nitrates may also be given to help dilate vessels and help relieve heart failure symptoms post-MI. Angiotensin-converting enzyme (ACE) inhibitors also help to dilate blood vessels, reducing blood pressure. Surgical intervention may also include installing a left ventricular assist device (LVAD), which can aid in pumping the heart (Minicucci et al., 2011).

In order to help prevent another cardiac event, as well as adverse remodeling effects, several drugs may be used chronically that have been proven effective against remodeling. These include ACE inhibitors, antiogensin-II receptor blockers, and β-andrenergic blocking agents, or β-blockers. Other treatments include stem cell therapy as well as surgically inserting a defibrillator (Minicucci et al., 2011).

By using molecular imaging, oxygen metabolism as well as potential myocardial viability may be observed as responses to treatments and therefore can help give personalized patient care to achieve the best outcome possible. As molecular imaging technologies advance, the ability to specifically deliver drugs to desired areas can help improve post-MI treatments.

2.3 Imaging Modalities

2.3.1 Positron Emission Tomography

PET is a noninvasive imaging technique that requires a radioactively labeled material, known as radiotracers or radiopharmaceuticals, to visualize metabolic states. This imaging modality is commonly used for molecular imaging, as it is useful for disease monitoring since diseases are metabolically active. The lack of anatomical reference, however, requires it be used in conjunction with either MR or CT.

PET scans use radiation in the form of positrons (β^+), which are produced in the nucleus of a nuclide that contains an imbalanced number of protons to neutrons. When this type of nuclide decays, the excess proton is released as a positron and a neutrino. The neutrino does not interact with its surroundings, but the positron interacts with electrons, causing annihilation. With annihilation, the positron and electron become γ ray photons and emit 511 keV of energy each while traveling in opposite directions (Mikla and Mikla, 2014). Scintillation detectors, single crystals that deposit γ rays and in turn convert them into scintillation photons, detect the photons emitted after an annihilation event (Melcher, 2000).

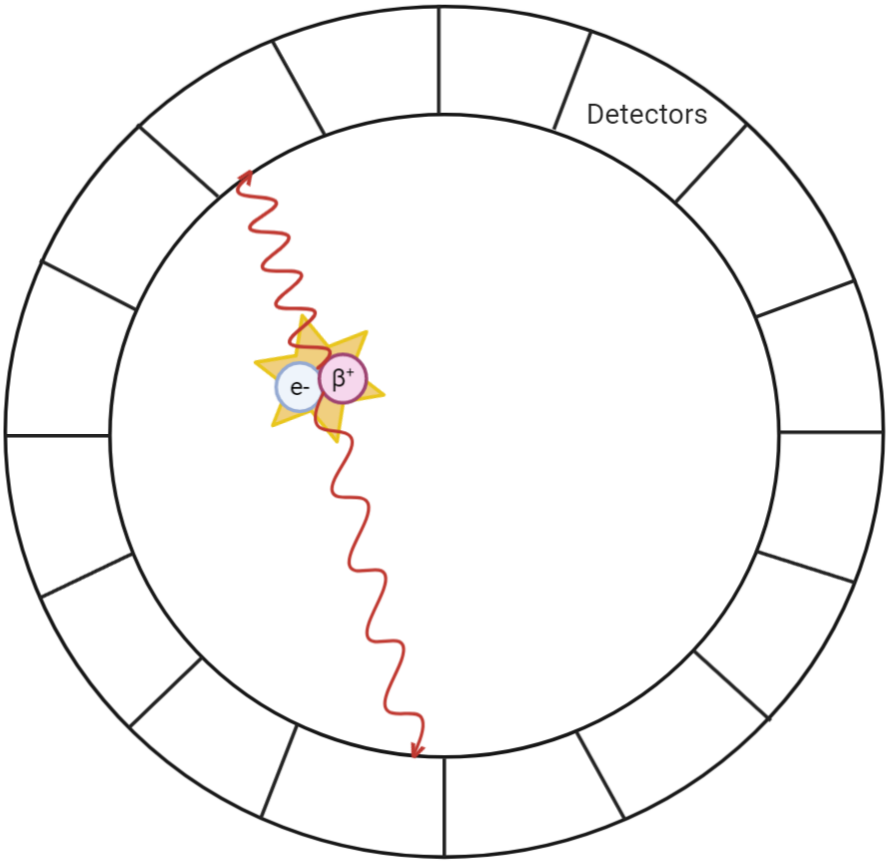

Figure 1. Visualization of annihilation event in PET imaging. An electron (e^-) and positron (β^+) interact and convert to photons, emitting 511 keV each as they travel in nearly opposite directions until they hit a detector along the ring of detectors. Created on Biorender.com.

As annihilation events send photons in almost opposite directions, the detectors have near-simultaneous detections after annihilation. When detected at nearly identical times, this is known as a coincidence event and the signals are then used to localize the point of annihilation. Photomultiplier tubes generate an electrical signal from the photons. This signal is then used to detect the point of annihilation using a line of response. Many of these lines of responses coming from different directions allow for tomographic acquisition of the radioactivity. Algorithms are then used to reconstruct the images and determine which points have the highest radioactivity accumulation (Spanoudaki and Levin, 2010).

Common radionuclides used in PET imaging that emit positrons include ^{18}F, ^{11}C, ^{64}Cu, ^{89}Zr, ^{124}I, and ^{68}Ga. Of these radionuclides, ^{68}Ga is the only one that is commonly produced by a

generator, eliminating the need for a cyclotron. This allows for convenient implementation in a radiochemistry lab. Additionally, apart from ^{11}C, ^{68}Ga has the shortest half-life at 67.7 minutes, which decreases the radiation exposure to a patient. Furthermore, ^{68}Ga has an 89% positron yield, favorable for PET imaging as more positrons can help provide a clearer image (Velikyan, 2018; Silvola et al., 2011). These qualities make ^{68}Ga a favorable radionuclide to work with for PET imaging.

When using a radiotracer for PET imaging, molar activity (A_m), the amount of radioactivity in the amount of radiotracer end product, including non-radioactive biproducts, should be high. By increasing the A_m, smaller amount in terms of molarity of these radiotracers are required; this is particularly of great importance in pre-clinical imaging of small animals, as they need higher doses to get enough signal to combat background noise (Sergeev et al., 2018).

To quantify the activity of a radiotracer to the site of interest *in vivo*, the highest maximum target-to-background ratio (TBR) is used. For measuring activity in plaques within the aortic arches, the target is the aortic arch uptake and the background is the blood flow present in the aortic arch. The activity within the region of interest, known as standardized uptake value (SUV), is used to calculate the highest maximum TBR and is calculated as follows:

$$Standardized\ Uptake\ Value = \frac{Radioactivity\ Conentration}{Dose/Weight}$$

When calculating the SUV, the radioactivity concentration refers to the concentration of radioactivity within the tissue volume. When working with small animals such as mice, the units can be expressed as kBq/mL. This value is then divided by the administered dose of decay-corrected radioactivity per weight of the patient. In imaging of small animals, this would be expressed as kBq/g, therefore making the units of SUV g/mL. The SUV values are then used to calculate the highest maximum TBR by using the following equation:

$$Highest\ Maximum\ TBR = \frac{SUVmax,\ aortic\ arch}{SUVmean,\ vena\ cava}$$

Calculating the highest maximum TBR is thought to correct for blood flow uptake within the targeted area, therefore serving as a more accurate parameter to determine plaque-specific uptake in the aortic arch (Chen and Dilsizian, 2015).

PET imaging is advantageous for several reasons. As mentioned previously, using PET over CT or MR allows for biological and metabolic imaging, a feature that is essential for monitoring diseases. When combining PET with CT or MR, the anatomical component can be included and therefore the localization of observed metabolic activities can be done. When compared to SPECT, both imaging modalities provide 3D metabolic images, which are useful for visualization and understanding biological processes. SPECT, however, is measured by single gamma photons, where PET is measured by coincident events from the photons of annihilation. By using two points to detect the annihilation point, more localization information is provided by PET, giving it a higher spatial resolution of 2.5-6 mm to that SPECT at 8-15 mm (Livieratos, 2013; Li et al., 2013). PET also has higher sensitivity and temporal resolution that SPECT and the radiotracers used in PET, such as ^{18}F or ^{68}Ga at less than two hours, have shorter half-lives than those used in SPECT, such as ^{99m}Tc at nearly five hours, which gives the patient a lower radiation dose (Li et al., 2014).

The disadvantages of PET imaging include the lack of anatomical reference, however as previously mentioned, this can be addressed by combining PET with MR and CT. Another disadvantage is the potential time of the scan. While the type of scan and radiotracer used changes the time, it can take several minutes in addition to the time waiting for the radiotracer to distribute. Additionally, by administering a radiotracer, there is radiation exposure to the patient. The effects of radiation are detailed in the *Radiation* section.

2.3.2 Computed Tomography

Computed tomography (CT) uses X-rays to non-invasively construct an image that gives anatomical information. As PET imaging provides metabolic information, combining CT with PET and superimposing the results both scans gives metabolic information with anatomical reference in order to know the location form which the information from the PET scan is coming from.

The most common CT scanners are helical CT scanners, which acquire their data by rotating around the patient while continuously shooting X-ray beams and acquiring the information. Hundreds to thousands of detectors are used and work in the same way as those used in PET scans. Once the X-ray beam passes through the patient, the detectors, consisting scintillation crystals followed by photodiodes, take up the X-ray photon and convert it to an electrical signal (Mikla and Mikla, 2014). In order to acquire enough data and keep the patient's radiation dose as low as reasonably achievable, the detectors must be highly efficient, detecting at least 80% of the emitted X-rays; with improving efficiency and sensitivity of these detectors, scans are completed in the time it takes most patients to hold their breath (Overdick, 2006). Upon acquiring data, image reconstruction is done to correct for any patient movement as well as X-ray scatter. Iterative reconstruction is done to create the 2D or 3D CT scan image from the acquired data. To reduce the overall radiation exposure to patients, better reconstructive methods have been developed to correct for problems that arise with lower X-ray doses during scans, such as lower signal-to-noise ratios giving noisier images (Willemink and Noël, 2019).

When doing a PET/CT scan, the first step includes attenuation correction. Attenuation correction allows for changes in intensity due to scatter and absorption to be corrected, resulting in a more accurate anatomical image (Mikla and Mikla, 2014). When studied in the canine model, Chin et al. determined that attenuation correction was needed to get more accurate radiotracer activity measurements, as the respiratory movements misaligned the diaphragm and led to inaccurate activity results (Chin et al., 2003). When studied in mice, D'Ambrosio et al. found that radiotracer activity was underestimated by 20% prior to

attenuation correction, showing that attenuation correction must also be done in pre-clinical animal studies in order to achieve more reliable results (D'Ambriosio et al., 2013).

As previously mentioned, one of the advantages of CT scans is the acquisition of the image within the span of one held breath. This rapidness in image acquisition also reduces the time of radiation exposure. CT scans also provide 3D images, giving useful anatomical reference throughout the scanned area. With a high spatial resolution of 0.5-0.625 mm and a fast temporal resolution between 83-135 ms, this imaging modality is advantageous in many ways (Lin and Alessio, 2009).

Disadvantages of CT scans include the lower contrast resolution when compared to MR or PET (Lin and Alessio, 2009). Additionally, while the high temporal resolution allows for fast scans, there is still radiation exposure when using CT imaging, the effects of which are detailed below.

2.3.3 Radiation

Radiation is energy in the form of particles, such as α and β particles, or energy waves, such as γ or X-rays. Radioactivity is measured in the SI system as Becquerels (Bq; 1 Bq = 1 disintegration/second). While they have higher ionization potential, the α and β particles do not penetrate as deeply through the body as X rays and γ rays and therefore can be blocked more easily. Paper and skin block α particles and plastic glass and thick aluminum can block β particles. By contrast, thick metals like lead or steel can block γ and X-rays (Yamamoto, 2013).

Some types of radiation can be harmful. The effects caused by harmful radiation can be either stochastic or deterministic. As described by Bolus, when exposed to some dose of radiation over time, there may be observed side effects. Common sources of such background radiation can be indoor radon gas or soil. Due to the prolonged exposure and low radiation level, development of side effects, such as cancer, is random and happens seldomly. These are stochastic effects. By contrast, deterministic effects occur after higher levels of exposure

during shorter periods of time. Ionizing radiation usually causes these non-stochastic, deterministic effects. These effects are known and can be expected after certain levels of radiation exposure. Ionizing radiation may affect the cell directly by damaging either proteins or DNA with single- or double-strand breaks, or indirectly by hydrolysis of water molecules within the cell, yielding free radicals and eventually peroxide hydroxyl molecules, which lead to a lack of enzymes in the cell. Both direct and indirect interactions by ionizing radiation lead to cell damage and death (Bolus, 2001).

There are different ways of measuring radiation exposure. As defined by the International Commission on Radiological Protection, the first is the absorbed dose, which measures the total energy from the radiation and is expressed in gray (Gy). As tissues and their properties vary between organs, the second measurement evaluates the radiation dose per tissue or organ. This is known as the equivalent dose and is measured in sieverts (Sv; J/kg). The last measurement is the effective dose, which adds all the equivalent doses of the different tissues or organs and is also expressed as Sv (ICRP, 2007).

As mentioned previously, there is known radiation exposure with the use of PET/CT imaging. When using PET imaging, the radiation is in the form of β^+ particles that convert to γ photons. This radiation is administered into the body of the subject being imaged. The amount of radioactivity from a PET scan varies depending on the radiotracer used and the quantity used. In a CT scan, X-rays cause radiation exposure to patients. As is the case with PET scans, the radiation exposure of a CT scan varies depending on the type of scan done. When measuring various methods of whole-body scanning in patients with 370 MBq [^{18}F]FDG, the total effective dose was shown to be between 13.45 and 32.18 mSv, which is between five and 13 times higher than the 2.4 mSv calculated annual effective dose from background radiation (Huang, Law, and Khong, 2009). In order to make sure the effective dose of the scan is as low as possible, the CT image may be limited to a certain area if possible, therefore reducing unnecessary exposure. As there is unavoidable radiation exposure with PET/CT scans, the risk of this must be outweighed by the potential benefits before imaging in order to limit unnecessary radiation exposure.

2.4 Autoradiography

Autoradiography (ARG) is a technique used to localize radionuclides in *ex vivo* and *in vitro* tissues of interest. Macroautoradiography is done when the tissues of interest have a larger area, such as cyosectioned organs on a slide. While there are many ways to do autoradiography, the method used in this project included phosphor plates. As detailed by Barthe, Maîtrejean and Cardona, these phosphor plates are usually comprised of small barium fluorobromide and divalent europium that form a lattice, where spots at which bromine is absent serve to trap electrons (Barthe, Maîtrejean and Cardona, 2012).

Once the tissue of interest is radioactive and prepared, either from *ex vivo* sectioning after PET imaging or *in vitro* incubation in the radiotracer, it is placed in very close proximity to the phosphor plate where exposure occurs; the process is shown in Figure 2. During this exposure, the radiation from the tissue ionizes the europium, which releases electrons that deposit into the bromine vacancies within lattice of the phosphor plate. By excitation with a laser beam in a scanner, the electrons are released from the vacancies and upon interacting with europium, the europium releases energy in the form of UV photons as it goes back to its divalent ground state (Barthe, Maîtrejean and Cardona, 2012). This release of UV photons is digitalized, providing a digital image showing the localization of the radioactive source.

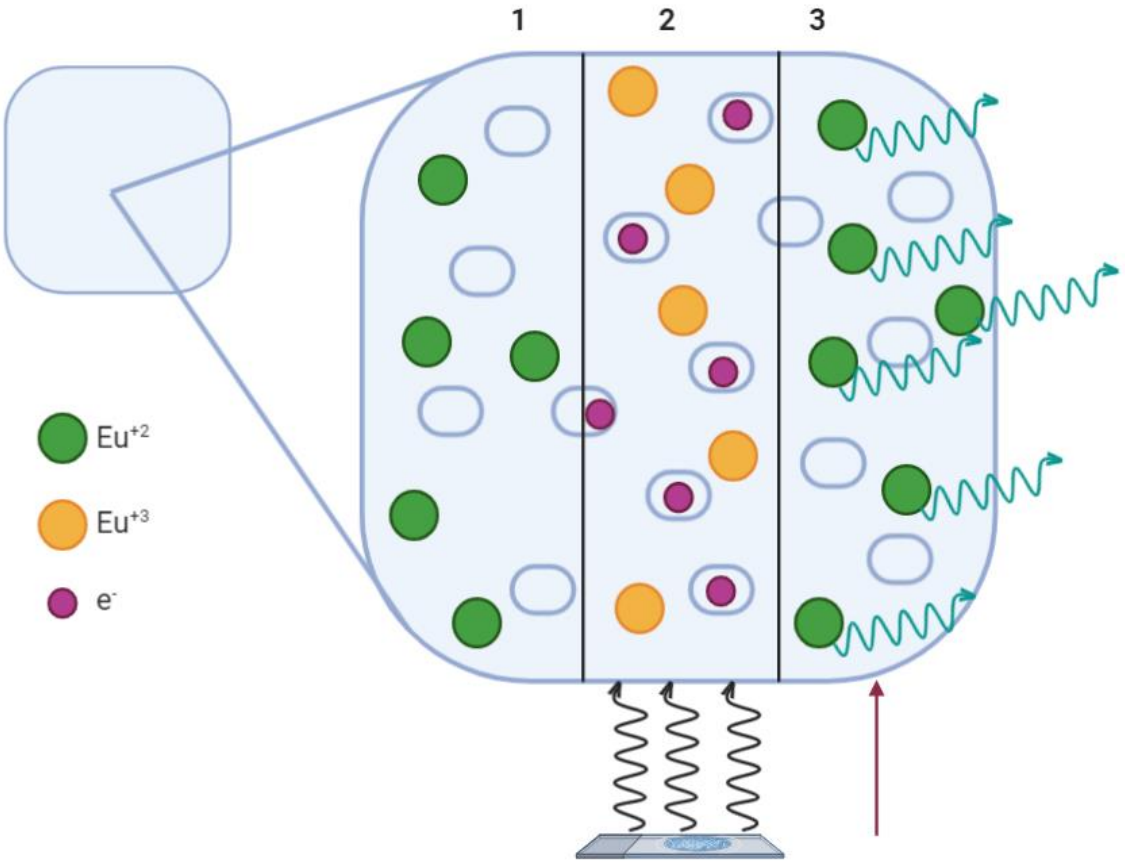

Figure 2. Principle of phosphor screen autoradiography, image is not to scale and has been adapted from Barthe, Maîtrejean and Cardona, 2012. (**1**) Basic phosphor plate lattice with bromine vacancies and ground-state divalent europium (Eu^{+2}). (**2**) Radioactive tissue of interest is placed close to the plate for exposure. As exposure occurs, the radiation releases an electron from the europium, becoming Eu^{+3}, and the electron fills a bromine vacancy. (**3**) Upon excitation from a laser in a scanner, electrons filling bromine vacancies are released and interact with europium, which goes back to its Eu^{+2} ground state, releasing energy as photons. These photons are captured and converted to electrical signals by the scanner to build a digital image. Created on Biorender.com.

2.5 Radiotracers

When developing a radiotracer for molecular imaging, there are several factors to consider, as detailed by Chen and Chen. An ideal radiotracer for targeting a molecule should be relatively easy to produce in a financially accessible way. It should be able to bind specifically to the target with high affinity, reducing uptake in unwanted tissues and binding

quickly to the desired target, thereby increasing the uptake and giving a better signal. Additionally, the radiotracer should bind quickly to the target and release slowly afterwards, while hardly binding to and having fast clearance from unwanted tissues, giving a high contrast ratio that would allow for high signal in desired areas with low background noise. The radiotracer should be highly sensitive when binding to desired tissues, reducing the amount of radiotracer needed for uptake. Furthermore, the radiotracer should be stable *in vivo*, with no biological factors affecting its structure, as well as have little or no toxicity (Chen and Chen, 2010).

Folate describes folic acid and related compounds with biological activity of folic acid. Folic acid is a B-vitamin that is essential in proper cell growth. The primary function of folate coenzymes involves 1-carbon reactions, either accepting or donating one carbon in various processes, such as: Amino acid metabolism, purine, pyrimidine, and thymidylate synthesis, and producing S-Adenosyl methionine, the body's main methyl donor that is involved in DNA methylation and over 100 other metabolic reactions (Doucette and Stevens, 2001). After absorption, folic acid is transported mainly as 5-methyl-THF (5-MTHF) bound to albumin in the plasma. To enter cells, the monoglutamate form is taken up by one of two mechanisms: *reduced folate carriers* or *folate receptors (FR)*, the latter being expressed only in limited tissues, since reduced folate carriers take up necessary folates (Doucette and Stevens, 2001). As one of the tissues expressing FRs are active macrophages, this is an interesting target for imaging inflammation (Jager et al., 2012).

To date, a few radiotracers have been developed to target atherosclerotic inflammation using PET imaging. The most common clinically used radiopharmaceutical has been 2-deoxy-2-[^{18}F]fluoro-*D*-glucose, or [^{18}F]FDG, which gives strong signals from plaques, however it can also give unwanted signals from other tissues, as it is not specific to inflammatory tissues. Additionally, this can be an inconvenience to patients, as they are asked to fast for long periods of time to avoid other unnecessary uptake in muscles and higher-than-normal blood glucose ranges that can alter signals (Hyafil and Vigne, 2019).

[^{68}Ga]Ga-[1,4,7,10-tetraazacyclododecane-1,4,7,10-tetraacetic acid]-(Tyr^3)-octreotate, or [^{68}Ga]Ga-DOTATATE, targets somatostatin receptors, which are overexpressed in

macrophages, and has also been studied clinically. It seems to have high specificity for the somatostatin receptor 2, which can be useful (Tarkin et al., 2017). Another clinical study using [^{68}Ga]Ga-DOTATATE demonstrated the tracer's ability to be taken up in calcified plaques in the left anterior descending coronary artery while having lower myocardial uptake than [^{18}F]FDG, giving more clarity of the plaques when imaging (Rominger et al., 2010). An additional tracer studied pre-clinically in mice and rabbits is aluminum fluoride-18 labeled NOTA-conjugated folate, or ^{18}F-FOL. This tracer targeted FR-β in atherosclerotic lesions and seemed to provide high specificity for imaging (Silvola et al., 2018).

Several radiotracers have been developed for imaging of MI, such as [^{68}Ga]Ga-DOTA-E-[c-(RDGfK)]$_2$ and [^{68}Ga]Ga-NODAGA-exendin-4. The first uses an RG (arginine-glycine-aspartic acid) peptide to target integrins present post-MI for evaluating extra-cellular matrix changes, while the latter targets expression of glucagon-like peptide-1 receptor (GLP-1R), a receptor that has cardioprotective effects when activated, post-MI (Kiugel et al., 2014; Ståhle et al., 2018). [^{68}Ga]Ga-DOTATATE has also been shown to target post-MI residual inflammation via somatostatin receptors, as mononuclear phagocytes undergo changes after this cardiac event that lead to the macrophages remaining long after the scar tissue has been formed, which can contribute further to tissue remodeling and heart failure (Tarkin et al., 2019; Ismahil et al., 2014). While uptake of [^{68}Ga]Ga-DOTATATE in the myocardium did not prove to be significant in mice, clinical evidence in humans counters this as the tracer identified recent MI inflammation with low myocardial binding as well as old injuries from previous cardiac events, though the latter remains histologically unverified (Thackeray et al., 2015; Ismahil et al., 2014).

2.6 [^{68}Ga]Ga-NOTA-Folate

[^{68}Ga]Ga-1,4,7-Triazacyclononane-*1,4,7*-triacetic acid (NOTA)-Folate, hereon referred to as [^{68}Ga]Ga-NOTA-Folate, is a radiotracer developed with a ^{68}Ga-labeled NOTA chelate attached to folic acid. Being a bifunctional chelating agent, NOTA can both bind to metals, such as gallium, while still having a reactive functional group, allowing for binding to other molecules of interest for targeting, such as folic acid (Brechbiel, 2007). The NOTA chelate

can form a thermodynamically and kinetically stable complex with metals, as well as be more lipophilic than other similar chelators, such as DOTA (1,4,7,10-Tetraazacyclododecane-1,4,7,10-tetraacetic acid) (Studer and Meares, 1992).

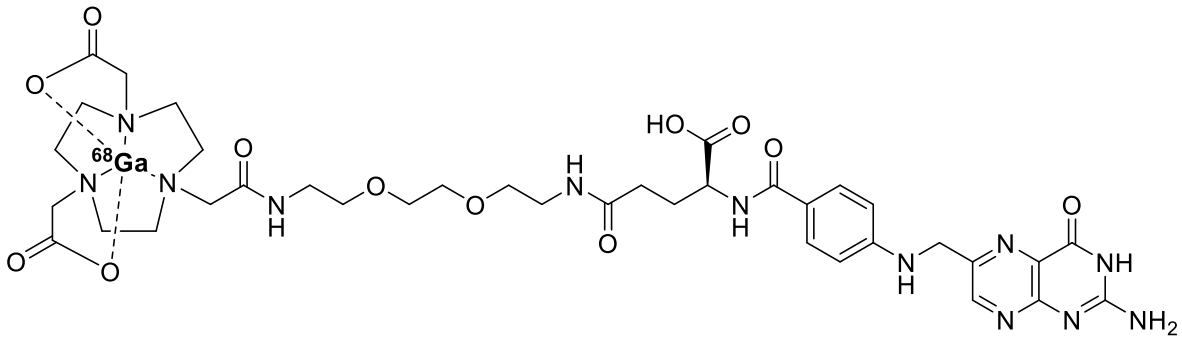

Figure 3. [^{68}Ga]Ga-NOTA-Folate structure.

Because of these properties, [^{68}Ga]Ga-NOTA-Folate has been studied *in vivo* in mice with xenografted FR-positive squamous cell carcinoma KB tumor cells, showing uptake in tumor cells with significantly lower uptake in the kidneys when compared to ^{68}Ga-DOTA-Folate. The NOTA complex was also more biochemically stable than the DOTA complex. When folic acid was added to block the FRs prior to tracer injection, the tumor uptake was significantly reduced by about 85%, showing the receptor-specificity of the tracer (Aljammaz et al., 2014). When compared to [^{99m}Tc]EC20, another FR-targeting imaging agent, [^{68}Ga]Ga-NOTA-Folate was shown to have similar tumor uptake levels with significantly lower liver uptake and blood activity levels, proving to have better biodistribution *in vivo* (Brand et al., 2017).

While these studies have shown [^{68}Ga]Ga-NOTA-Folate to be a suitable tracer for tumor detection, there is a lack of research done to assess the tracer's ability to target FR-βs and image other inflammatory diseases. Given the tracer's success with targeting the FRs in tumor cells, it is of high interest to see whether this same specific targeting can apply to FR-βs present in active macrophages for detecting and imaging inflammation. While many diseases cause inflammation, the two disease models studied will be atherosclerosis in mouse and human tissues, as well as myocardial infarction in rats.

2.7 Radiochemistry Analysis Methods

Radiochemical purity is the level of which the end product synthesized is indeed what it is supposed to be, compared to other biproducts or impurities that may have been made in the synthesis process.

2.7.1 High Performance Liquid Chromatography

Analytical high performance liquid chromatography (HPLC) is a method used for quality control analysis, as it distinguishes a chemical's physical and structural properties (Crowley, 2020). HPLC requires a column through which solvents and the chemical of interest, or analyte, pass. When using reversed-phase HPLC, the column's stationary phase, comprised of unbranched alkanes, is nonpolar and the solvent passed through, or its mobile phase, is polar (Bélanger, Paré and Sigouin, 1997).

Separation can occur based on several factors, such as the size, charge and polarity of the chemical being observed in addition to the viscosity of the solvent used (Bélanger, Paré and Sigouin, 1997). The solvents and columns used should be specific to do the appropriate separation for chemical identification. The column used for QC in this project was a Jupiter Proteo C18 column, with the particle sizes of 5, 5, 10 and 15 μm, and pore size of 300 Å. Being a C18 column, the alkanes in the stationary phase are 18 carbons long and are linked to spherical silica particles of the sizes listed above. Additionally, the pore size of 300 Å refers to the pores within the silica particles. This size is designed to help separate larger molecules. The solvents were used in a gradient fashion, changing the amounts used as the QC was being done. The mobile phase solvents included hydrophilic water with 0.1% TFA and hydrophobic pure acetonitrile. The TFA buffer is added to the water to fully protonate any acidic analyte, as full protonation increases molecule stability (Crowley, 2020).

The pump in the HPLC system pumps the solvents through the column, creating pressure that pushes the analytes through the column. As the column is hydrophobic, analytes that are relatively more hydrophobic and less polar will interact more, passing through the column

slower than more hydrophilic and polar analytes. This in turn separates the analytes. The retention time of an analyte, or the time it takes to pass through the column, is measured and varies depending on its size and polarity, with smaller molecules traveling faster through the column than larger ones (Crowley, 2020).

Data from HPLC is given as a chromatogram where the x-axis is the time of the QC run and the y-axis is the radioactivity detected in counts per second (CPS). As a compound is pushed through the column, its radioactivity will be measured, as will its retention time within the column. This produces a peak in the graph. The purity of [^{68}Ga]Ga-NOTA-Folate may be assessed using HPLC, as any impurities in the form of free ^{68}Ga being smaller and highly polar travel faster through the column and therefore produce its own peak. Being highly sensitive and able to give QC results within a few minutes, HPLC is an efficient and reliable method to assure radiochemical purity.

2.7.2 Instant Thin Later Chromatography

Instant thin layer chromatography-silica gel (iTLC) is one of the techniques used to quickly evaluate the radiochemical purity of a radiopharmaceutical. The iTLC plate can be made of a few components, including glass or aluminum foil. For iTLC, there is a stationary phase, a mobile phase, and a solute. The iTLC strips used in this project were made from paper coated with silica gel, making this adsorbent compound the stationary phase. Other examples of materials for stationary phase include cellulose or aluminum oxide. The mobile phase is the solvent or developer in which the iTLC strip is placed. The product being evaluated is the solute.

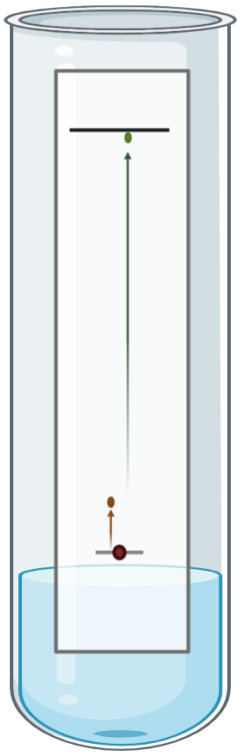

Figure 4. Visualization of compound separation on iTLC strip. The solute is placed as a small dot on the line drawn. The strip is placed in the development chamber, where the developer is pooled below the line containing the solute. As the developer moves up the strip's capillary network, the components within the solute are separated based on various properties depending on the conditions used. In this example, the strip has silica gel coating and the developer is a slightly acidic buffer. As the buffer travels up the network, the most polar substance binds first to the silica in the coating, therefore traveling to the solvent front, shown as the black line at the top of the strip, first. The less polar compound remains at the bottom of the strip, as most of the silica gel has already been bound. Created on Biorender.com.

When doing iTLC, a small amount of the solute is placed on a small pencil marking made on the strip, then the strip is placed into the development chamber, which has the solvent pooled at the bottom at a level lower than the solute. The solvent front, a line drawn in marker drawn towards the top of the strip, marks the endpoint of the separation. As it is drawn in ink, it leaves a bleeding trail as it travels up the strip via the developer. The strip's stationary phase has a capillary network which allows for the solute and mobile phase to compete for binding to the stationary phase, going up the strip and separating by different properties in the process, as visualized above in Figure 4. One such property is polarity. As silica gel is polar, the most polar substance will interact quicker and faster with the stationary phase,

traveling fastest up the strip. By interacting first with the stationary phase, substances with higher polarity leave less polar substances to interact with the stationary phase, therefore they do not travel as high. Differing substance properties, such as size, polarity, lipophilicity and charge, separate at different rates and can be identified (Bele and Khale, 2011; Decristoforo et al., 2007).

iTLC is useful for assessing radiochemical purity in an end product, as it can quickly separate the impurities from the desired product based on differing properties. The process can be done relatively quickly, and as time is critical when working with radionuclides, it serves as a reliable method for quality control of some radiopharmaceuticals (de Oliveira et al., 2011).

3 AIMS AND HYPOTHESES

The first aim of this project was to synthesize [^{68}Ga]Ga-NOTA-Folate with high purity, yield, and molar activity. When done properly adhering to the protocol, it was hypothesized that the end product would be made meeting the aimed criteria.

The second aim of this project was to biologically evaluate [^{68}Ga]Ga-NOTA-Folate in atherosclerosis and MI disease models. The atherosclerotic model was assessed using *in vivo* PET/CT imaging with the atherosclerotic mouse model on a high-fat diet and control mouse model fed regular chow. Then, tissue sections from mouse aortas were used to evaluate the *ex vivo* binding ability of the tracer to the atherosclerotic lesions present. Upon analyzing, it was hypothesized that radioactivity should be present in high concentrations in the atherosclerotic lesions co-localizing with FR-β-positive macrophages. Additionally, [^{68}Ga]Ga-NOTA-Folate was used to analyze *in vitro* binding to atherosclerotic plaques in human carotid artery tissue sections using total and blocked tracer binding techniques. It was hypothesized that the total binding tissues will have high radioactivity in the atherosclerotic lesions, while the blocked binding tissues will have little to no radioactivity.

To biologically evaluate specific binding of [^{68}Ga]Ga-NOTA-Folate to FRs in the MI model, heart tissues from rats that had undergone surgically-induced MI operation were used for *in vitro* imaging using the autoradiography technique, or ARG. Half of the tissues were incubated with the tracer alone, while half were incubated with FR-specific folate glucosamine as a blocker. It was hypothesized that this tracer will show high radioactivity in the areas containing inflammation lesions with high specificity in the tissues with total tracer binding, and little to no radioactivity in inflammation lesions in the tissues having been exposed to the blocker.

4 METHODS AND MATERIALS

4.1 Radiosynthesis of [^{68}Ga]Ga-NOTA-Folate

This radiosynthesis protocol was done six times, with the first being used as a test for metabolite analysis, the next four being used for a total of two injections for *in vivo* imaging in mice each, and the final being used for *in vitro* binding of the tracer to rat MI tissues. The generator scheme for the syntheses is detailed in Figure 5.

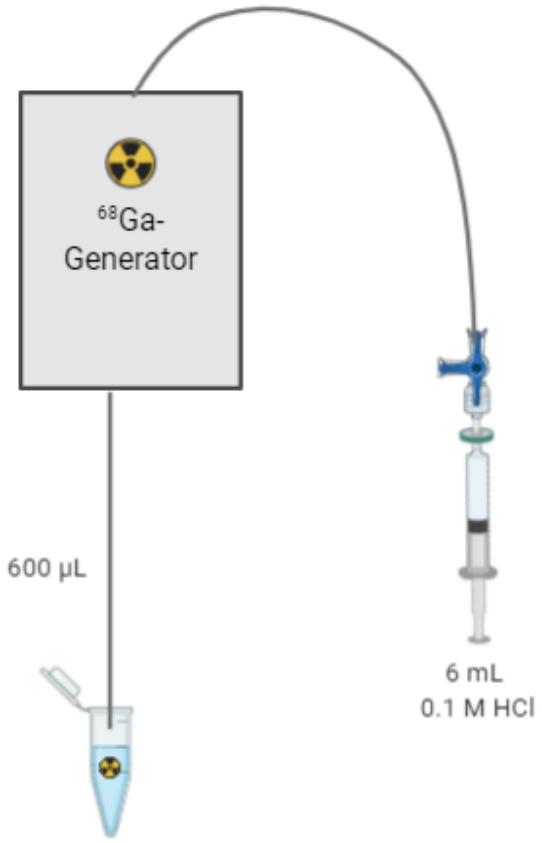

Figure 5. Generator scheme for radiosynthesis of [^{68}Ga]Ga-NOTA-Folate used in *in vivo* and *in vitro* experiments. Created on Biorender.com.

For *in* vivo studies with two mice being imaged one hour apart, the ordered amount of [^{68}Ga]Ga-NOTA-Folate for proper imaging with the Molecubes camera was 52 MBq, with a

desirable concentration of 330 MBq/mL. Within 24 hours prior to the radiosynthesis, the gallium generator (IGG1000; Eckert & Ziegler, Berlin, Germany) was eluted with 10 mL of 0.1 M HCl in order to remove any potentially accumulated metal impurities. Once this was completed, the radiosynthesis procedure began by combining in the reaction vial 60 mg of HEPES (2-[4-(2-hydroxyethyl)piperazin-1-yl]ethanesulfonic acid; Merck, Darmstadt, Germany) with 50 µL of TraceSELECT water (Honeywell, Bucharest, Romania), 10 µL of 0.1 M gentisic acid (2,5-dihydroxybenzoic acid; Sigma-Aldrich, Darmstadt, Germany), prepared by diluting 10 mg of gentisic acid in 650 µL of TraceSELECT water then vortexed until dissolved, and stock solution 20 µL (0.5 nmol/µL) of NOTA-Folate precursor (a gift from Professor Philip Low, Purdue University, USA) for total a precursor amount of 10 nmol. Then 6 mL of 0.1 M HCl were eluted through the generator at a rate of about 2 mL per minute, stopping briefly halfway to collect a 0.6 mL fraction after about 2.4 mL have been eluted. From the fraction collected, 0.5 mL was then transferred to the reaction vial and vortexed before 10 minutes of incubation at 80° C. After incubation, the reaction vial was cooled in ice for 2 minutes and 55 µL of 1 M NaOH are added to raise the pH to around 5-7. The final radioactivity was measured, and a diluted sample of the product was used for high-performance liquid chromatography (HPLC) quality control (QC) analysis. As the QC was done, the final [^{68}Ga]Ga-NOTA-Folate product was sent for delivery to BioCity. Upon completion of a successful QC, the product could then be injected into the mice.

The QC was done using analytical HPLC with a Jupiter Proteo C18 column, 5 µm 300 Å 150 × 4.6 mm and UV set to 254 nm. Solvent A was Milli-Q water (182 Ω) with 0.1% trifluoroacetic acid (TFA; Merck, Darmstadt, Germany) and solvent B was acetonitrile with 0.1% TFA. The method used was ^{68}Ga-NOTA-Folate QC and is as follows:

Time Point	**Solvent A (%)**	**Solvent B (%)**	**Flow Rate**
0 minutes	97	3	1 mL/minute
14 minutes	65	35	1 mL/minute
14.1 minutes	68	32	1 mL/minute
14.2 minutes	71	29	1 mL/minute

14.3 minutes	74	26	1 mL/minute
14.4 minutes	77	23	1 mL/minute
14.5 minutes	80	20	1 mL/minute
15 minutes	97	3	1 mL/minute

4.2 Optimization of Concentrated [^{68}Ga]Ga-NOTA-Folate Radiosynthesis Procedure

The protocol for the radiosynthesis of concentrated [^{68}Ga]Ga-NOTA-Folate using an SCX cartridge was tested for optimal NOTA-Folate precursor concentration level. The generator scheme is detailed in Figure 6.

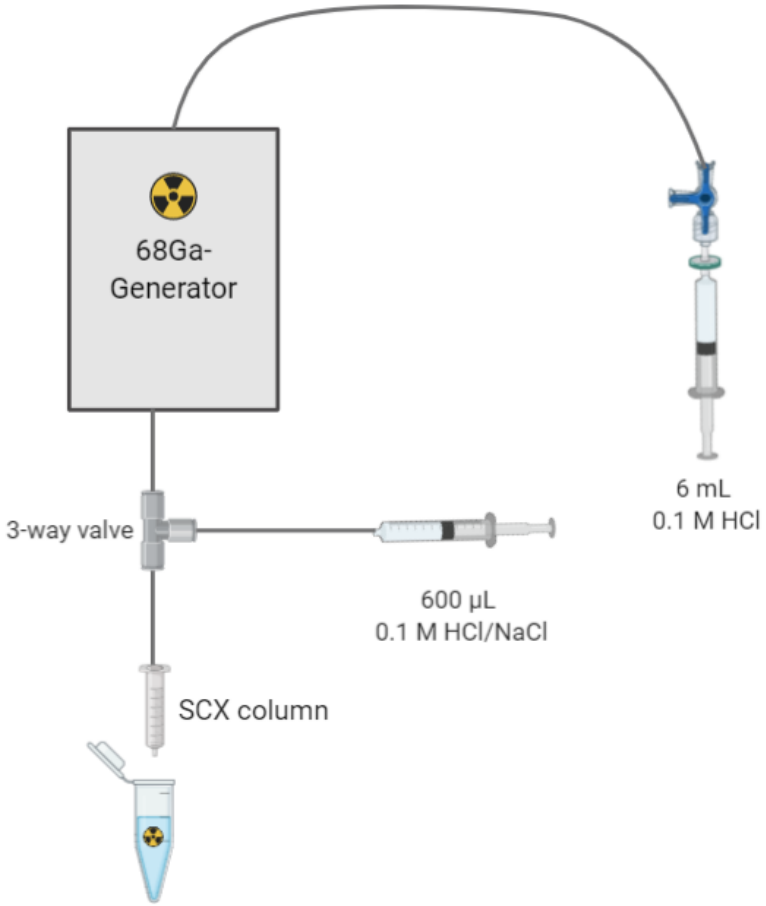

Figure 6. Generator scheme for concentrated [^{68}Ga]Ga-NOTA-Folate production using SCX column. Created on Biorender.com.

The initial protocol began with combining 66 mg of HEPES with 10 μL of 0.1 M gentisic acid, prepared as described previously, and the desired amount of 0.5 nmol/μL NOTA-Folate precursor and water added to total a volume of 50 μL in the reaction vial. Once this was prepared, 7 mL of 0.1 M HCl solution was eluted at a rate of 2 mL/min through the gallium generator and into waste, passing through a Strata strong cation exchange (SCX) column (Phenomenex, Torrance, CA, USA) in the process. The column was then moved to an empty vial and 600 μL of a 0.1 M HCl/1.0 M NaCl solution were slowly eluted through via the cartridge line at a rate of around 2 mL/min. Then, 550 μL of this free Gallium solution was added to the reaction vial and vortexed. Incubation occurred for 10 minutes at 40° C and 30 μL of 1.0 M NaOH was added at the end of the reaction to increase the pH level. The total radioactivity was measured and iTLC (Agilent, Santa Clara, CA, USA) was used to determine end product purity.

The different NOTA-Folate precursor concentrations were tested three times for each concentration; 10 nmol, 7 nmol, and 5 nmol of NOTA-folate. The amount of precursor added to the reaction vial was calculated accordingly per the stock precursor's 0.5 nmol/μL concentration, with TraceSELECT water being added to top up the 50 μL volume in the reaction vial. At the end of each synthesis, a small 1 μL portion of the end product was diluted in 100 μL of TraceSELECT water and 1 μL from this dilution was placed on three pre-cut iTLC strips. Each strip was then developed in 50 nM of citric acid ($C_6H_8O_7$) solution and upon reaching the marked top line, one of the strips was cut in half and measured separately for purity using the gamma counter (1480 Wizard 3"; Perkin Elmer/Wallac, Turku, Finland). The remaining two iTLC strips, along with another pre-cut iTLC strip, were used to visualize the QC using ARG. While two strips contained the diluted end product, one of those strips and the third strip each contained a small 1 μL portion of the free gallium solution previously collected, diluted in water at a level of 1:200. After development in citric acid, the strips were dried with a hairdryer and placed in a plastic bag before being placed in an exposure cassette for one hour. After this was done, the ARG imaging plate was scanned, as detailed in the *Ex Vivo Tissue Imaging* section below.

4.3 *In Vivo PET/CT Imaging*

Four 6-month-old low-density lipoprotein receptor deficient male mice only expressing apolipoprotein B100 ($LDLR^{-/-}/ApoB^{100/100}$) on high-fat diet were used as an atherosclerotic model and four 3-month-old C57BL/6N strain healthy male mice on regular feed were used as controls. Imaging was done using Molecubes X-CUBE and β-CUBE (Molecubes, Gent, Belgium). They were anaesthetized with isofluorane (Zoetis Finland Oy, Helsinki, Finland) via inhalation with an induction rate of 4-5% at an air flow of 400-500 mL/min, then maintained with 1.5-3% at a rate of 150-250 mL/min and injected via tail vein cannula with 100 µL of eXIA 160 XL contrast agent (Binitio Biomedical, Inc., Ottawa, Canada). They were then injected with 40-100µL of [^{68}Ga]Ga-NOTA-Folate (11.8 ± 0.7 MBq; 0.345 ± 0.05 MBq/kg i.v.). The mice were imaged individually first with the X-CUBE for CT imaging, then the β-CUBE for 40 minutes of dynamic PET and high-resolution CT imaging. The mice were then sacrificed at 60 minutes post-injection and their organs were collected and weighed in pre-weighed tubes, as well as measured using a gamma counter. The aortas were taken to the Histocore facility in Medisiina D, where they were sliced for tissue staining and autoradiography analysis.

4.4 Ex Vivo Tissue Imaging

The aortas were taken directly to the Histocore after imaging, where they were sliced into 20 µm and 8 µm sections. The slides containing the tissues were placed on an erased imaging plate (Fujifilm, Tokyo, Japan) and left for two hours of exposure time. Once this was completed, the imaging plates were scanned using the Fuji Film BAS-5000 scanner (Fuji Tokyo, Japan; internal resolution of 25 µm) and saved as digital images in .inf and .img formats. Following this, the 20 µm slides were frozen until they were taken for H&E staining at the Histocore. Once the tissues were stained, they were scanned using the Pannoramic 1000 scanner (3DHistec Ltd., Budapest, Hungary) and saved as digital images. Using the ARG and H&E images, analysis was done using Pannoramic Viewer, GIMP 2.0 and TINA softwares as detailed under *Image Analysis*.

4.5 Metabolite Analysis In Vitro

The first metabolite analysis was done *in vitro* on frozen plasma taken previously from a rat to verify the protocol method with precipitation and HPLC analysis. The sample was defrosted overnight in a 4° C refrigerator, then 1 mL was incubated at 37° C for five minutes. After this, 2.04 MBq of [^{68}Ga]Ga-NOTA-Folate was added to the plasma and vortexed. The plasma was then incubated once more at 37° C with 200 µL samples being taken at each of the following time points: 10, 20, 40, and 60 minutes. Once a sample was taken at a certain time point, it was placed in ice to cool, then 200 µL of acetonitrile was added before being vortexed then centrifuged at 4500 rpm for 3 minutes. The supernatant liquid was then separated into a new Eppendorf tube that was previously weighed. The supernatant sample was then weighed and 250 µL was then filtered through a 0.45 µm Minispike filter (Waters Corporation, Milford, MA, USA). This filtration was done to avoid any large molecules in the plasma from going into the HPLC column. The remainder of the unfiltered supernatant liquid was then diluted with 1 mL of 0.1% TFA and 1 mL of this, with a CPS value of 400, was used in HPLC metabolite analysis, detailed below. The remaining diluted liquid was then weighed and analyzed along with the leftover pellet using a calibrated gamma counter (1480 Wizard 3"; Perkin Elmer/Wallac, Turku, Finland).

The QC was done using analytical HPLC column as described in section 3.1 and/or with a semi-preparative C18 Jupiter column (250 × 10 mm, Phenomenex Inc., Torrance, CA, USA), with a rate of 5 mL/min, UV of 254 nm and radioactivity detection. Solvent A was Milli-Q water (180 Ω) with 0.1% TFA and solvent B was acetonitrile with 0.1% TFA. The method used was ^{68}Ga-NOTA-Folate-Metab-MGM and was as follows:

Time Point	**Solvent A (%)**	**Solvent B (%)**	**Flow Rate**
0 minutes	95	5	5 mL/minute
15 minutes	75	25	5 mL/minute
16 minutes	95	5	5 mL/minute

4.6 Metabolite Analysis In Vivo

In total, 11 metabolite analyses were done following the *in vivo* protocol. For the first two analyses, two tracer standard methods were done to determine the best one for future use. The first one done used 500 µL of previously frozen rat plasma. To this plasma, 500 µL of acetonitrile were added to precipitate the proteins. This combination was then vortexed and centrifuged at the same rate as detailed above, with the supernatant liquid then being transferred to a new Eppendorf tube.

The first tracer standard solution was made in a new Eppendorf tube with a few µL of [^{68}Ga]Ga-NOTA-Folate totaling 383 CPS, measured with a well counter, to which 200 µL of the supernatant liquid was added. Then, 850 µL of 0.1% TFA solution was added and the tube was vortexed. The 1 mL HPLC loop was washed with 2 mL of HPLC-grade pure acetonitrile (Merck, Garmstadt, Germany), then 2 mL of 0.1% TFA in water prior to the injection of 1 mL of the tracer standard solution. The HPLC analysis was done using the same settings as previously mentioned for the *in vitro* metabolite analysis.

The second tracer standard was done by combining a few µL of [^{68}Ga]Ga-NOTA-Folate totaling 405 CPS with 100 µL of acetonitrile and 900 µL of 0.1% TFA. Once combined, the solution was vortexed and 1 mL was injected into the HPLC for analysis after washing the loop with acetonitrile then 0.1% TFA as described previously. Following the comparison of HPLC results between the tracer standards, it was determined that the second method with only acetonitrile and TFA would be used as the tracer standard in the remaining analyses.

Following the analysis of the tracer standard with each radiosynthesis of [^{68}Ga]Ga-NOTA-Folate, another nine metabolite analyses were done in plasma collected after one hour of PET imaging of eight atherosclerotic mice with injected [^{68}Ga]Ga-NOTA-Folate. Upon collecting blood samples from the mice at 60 minutes post-injection, the plasma was separated through centrifugation at the same settings as previously described, then separated into a new tube. An equivalent amount of acetonitrile was added to the same tube to separate the proteins in the plasma. The plasma was then centrifuged twice with the same setting as previously described to assure the pellet and supernatant liquid were sufficiently separated. The

supernatant liquid was then separated into a pre-weighed Eppendorf tube and then weighed once more. Then, several µL of the supernatant were transferred to a new Eppendorf tube and measured in a well-gamma counter so that the total CPS was between 350-400 CPS, with a maximum limit of 200 µL. 0.1% TFA was then added and the tube was vortexed before being filtered using a 0.45 µm filter. Once the HPLC column was washed as previously described, 1 mL of the filtered sample was injected and analyzed using the HPLC protocol for metabolites. The leftover supernatant liquid was then weighed once more before being analyzed using the Wizard gamma counter alongside the corresponding pellet.

To ensure the difference in the metabolite and tracer peaks given their close proximity, one analysis was done using the supernatant sample from one mouse. The sample was prepared as described above, though an additional few µLs of the [^{68}Ga]Ga-NOTA-Folate were added before the filtration. One mL of this mixture was then injected into the HPLC and analyzed as detailed above in order to see if the metabolite peaks would change. This allowed for positive confirmation of the observed metabolite, as discussed under *Results*.

After completion of the analyses, the HPLC column was cleaned with 50% pure acetonitrile and 50% pure Milli-Q water at a rate of 5 mL/minute for 5 minutes, then 70% pure acetonitrile and 30% pure Milli-Q water at the same flow rate for 5 minutes. Once this was done, the column was stored until the next use.

4.7 In Vitro Blocked Binding Experiment In Human Carotid Arteries

Human carotid artery samples were used to assess the specificity of [^{68}Ga]Ga-NOTA-Folate to bind to FRs by *in vitro* blocking experiments. In total, two experiments were done, both following the same protocols with only a slight difference in the amount of radioactivity used. The cryosectioned tissues were first defrosted and pre-incubated in PBS buffer for 40 minutes. As this occurred, the radiosynthesis and QC testing of [^{68}Ga]Ga-NOTA-Folate was done as described in the *Radiosynthesis of [^{68}Ga]Ga-NOTA-Folate* section.

The tissues were then divided into two groups, one that was incubated in PBS with 0.2 MBq of [^{68}Ga]Ga-NOTA-Folate and the other that was incubated in PBS with 0.2 MBq of

[^{68}Ga]Ga-NOTA-Folate along with FR blocker folate glucosamine (MW 602 g) at a concentration 300 times higher than that of the tracer. Incubation was done in room temperature for 45 minutes. After this, the tissues were washed with cold PBS buffer twice, then twice again with extra-pure water. They were then dried, using a hairdryer to hasten the process, before being placed in a Fijifilm exposure cassette for 2.5 hours for ARG imaging. Upon completion of exposure, the imaging plate from inside the cassette was then scanned with the BAS-5000 scanner in the same manner previously described.

4.8 In Vitro Blocked Binding Experiment Rat MI Healing

To evaluate the ability of [^{68}Ga]Ga-NOTA-Folate to target inflammation corresponding to MI healing, frozen tissue sections from the hearts of rats having undergone an MI-inducing operation 3 days prior to euthanasia were provided by a colleague for one *in vitro* blocked binding experiment.

After taking the tissues from the freezer to defrost, they were incubated in PBS solution for 40 minutes. In the same manner as the previous section, the radiosynthesis and QC testing of [^{68}Ga]Ga-NOTA-Folate was done. The successful final product yielded 296 MBq, with an activity concentration of 466.7 MBq/mL and a specific activity of 29.64 GBq/μmol. Using previous *in vitro* studies as a reference, 0.9 MBq of the tracer was diluted in 50 mL of PBS. This solution was then split evenly into two 25 mL portions, each one with 0.45 MBq. From this value, the concentration of the tracer was determined to be 0.015 nmol per portion. Using this information, the folate glucosamine blocker was then made into solution with a concentration 500 times higher than that of the tracer. From this blocker solution, 37.5 μL were added to one portion of the PBS/tracer solution. Accordingly, 37.5 μL of PBS were added to the other portion to maintain the same volumes in both. The slides with tissues were put into two separate incubation boxes and covered with 16 mL each of their corresponding solution, one being designated for total tracer binding with no blocker added and the other with the solution containing the blocker. The tissues were incubated here for 45 minutes before being washed twice with cold PBS and extra-pure water. They were then dried and placed in an exposure cassette for ARG imaging. Following the 2.5 hour exposure, the imaging plate was scanned and saved.

4.9 Image Analysis

The *in vivo* PET images were analyzed using Carimas 2.10 software (Turku PET Center, Finland, www.turkupetcentre.fi/carimas/). The CT image served as anatomical reference in order to properly identify the regions of interest, which were the aortic arch and the vena cava, which served as an indicator of radioactivity in the blood. Once this was defined for every plane applicable, the maximum Bq/mL levels were calculated for the aortic arch. These values, along with those of the mean Bq/mL from the vena cava, were then converted to kBq/mL which then were used to calculate the SUV and the percent of injected radioactivity dose per mL of blood (%ID/mL) values for each animal. The SUV and %ID/mL for the final five time points of imaging, 600-2400 seconds, were averaged. From these averages, the highest maximum TBR was calculated. The TBR was then used to compare the experimental and control groups for differences in uptake in the aortic arch using an independent samples *t*-test.

In vitro and *ex* vivo images were analyzed using Pannoramic Viewer (3DHistec Ltd., Budapest, Hungary), GIMP 2.0 (www.gimp.org), and TINA (Ravtest Isotopemessgeräte, GmbH, Straubenhardt, Germany) softwares. The first step in analyzing the images was opening the H&E-stained scanned image on Pannoramic Viewer and exporting it as a TIFF file with a magnification setting of 1:64 to preserve the data and be able to zoom in for details later. Once it was exported and saved, the corresponding ARG image for the slide was opened and selected using TINA and exported as a TIFF file as well as saved as a PCBAS file to extract the image later. Once both the H&E and ARG images were saved, the H&E image was opened on GIMP 2.0 where it was then edited so that the aortas were contoured using the lasso selection tool. This was done to have the anatomical reference for the ARG images in order to properly identify regions of interest (ROIs) for analysis.

ROIs for mouse tissues, shown in Figure 7, included plaque in the aortic arch (pk), plaque in the brachiocephalic artery (pb), plaque in the carotid artery (pc), plaque in the subclavician artery (ps), plaque in the descending aorta (pl), healthy vessel wall (w), calcification (c), and adventitia (a). The ROIs for human carotid artery tissues included plaque (pl) and healthy

vessel wall (w). The ROIs for MI rat tissues, shown in Figure 8 included MI scar tissue (s) and healthy remote tissue (rem).

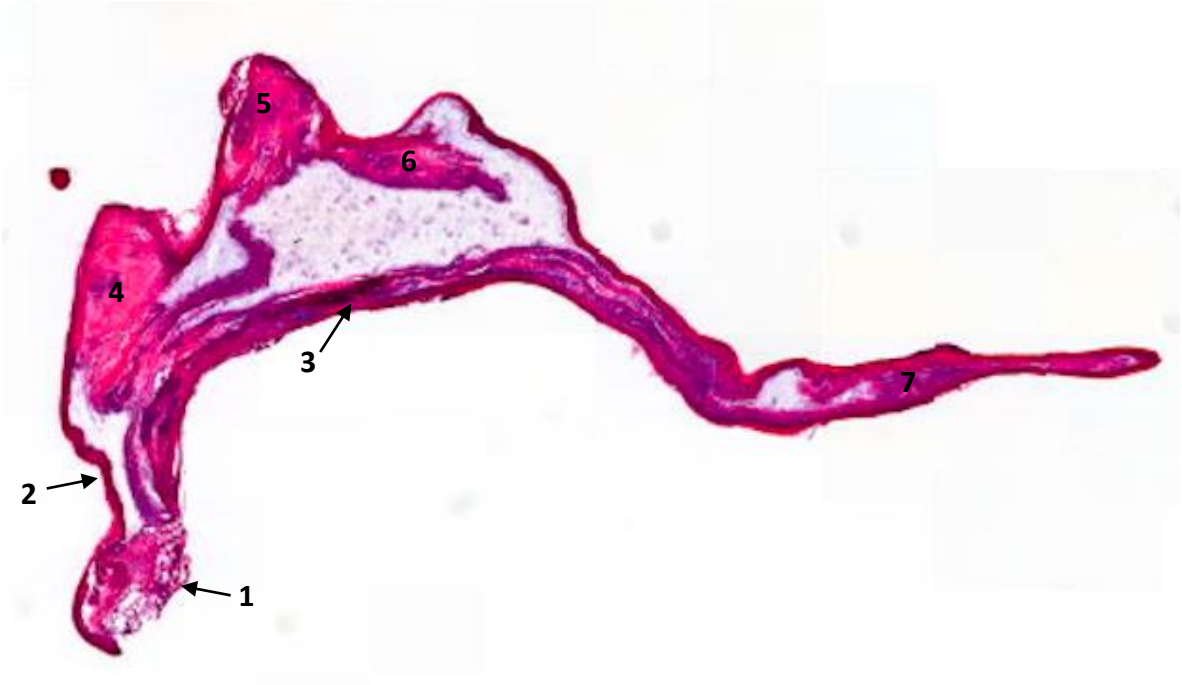

Figure 7. H&E stained aorta section from an atherosclerotic mouse with labeled ROIs: (**1**) adventitia; (**2**) wall; (**3**) plaque in aortic arch (pk); (**4**) plaque in the brachiocephalic artery (pb); (**5**) plaque in the carotid artery (pc); (**6**) plaque in the subclavician artery (ps); and (**7**) plaque in the descending aorta (pl).

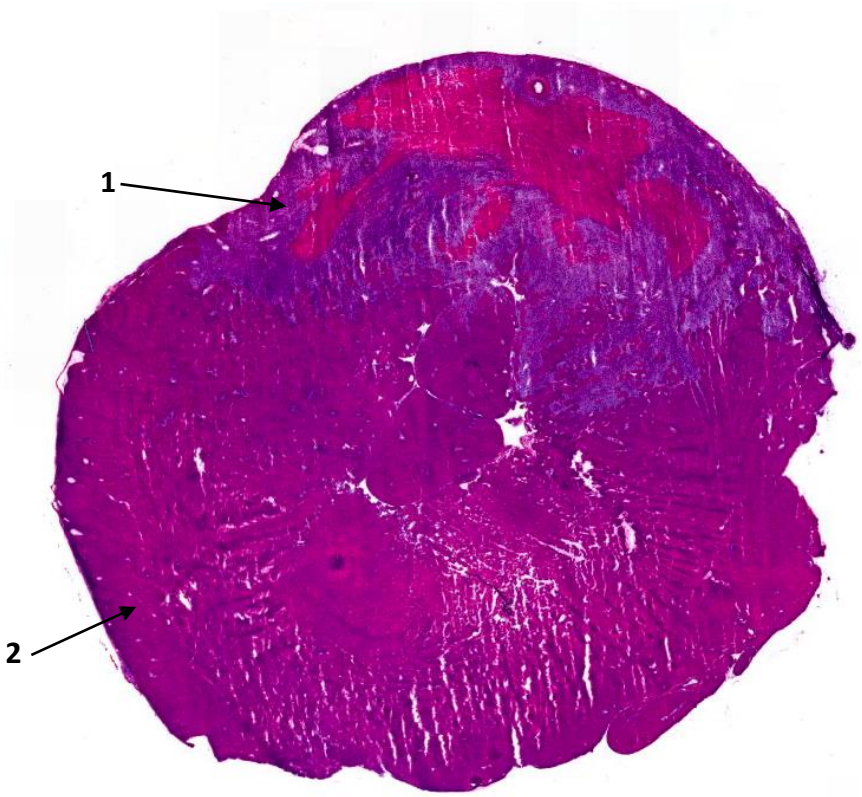

Figure 8. H&E stained rat heart 3 days after MI-inducing surgery with labeled ROIs: (**1**) MI scar tissue and (**2**) remote healthy tissue.

Once the H&E stained image had the aortas outlined with a contour, the contour was superimposed onto the ARG image, giving it an anatomical reference. This contoured image was then opened on TINA, where the ROIs would be drawn as closely as possible to the corresponding areas, which were seen at the same time in the magnified H&E image using Pannoramic Viewer. After drawing all ROIs, the data was then exported and statistically analyzed. The units used for expressing uptake of [^{68}Ga]Ga-NOTA-Folate were photostimulated luminescence per square millimeter, or PSL/mm^2.

4.10 Experimental Animals

As an atherosclerotic model, four 6-month-old low-density lipoprotein deficient mice expressing only apolipoprotein B100 (LDLR$^{-/-}$/ApoB$^{100/100}$) were used (strain #003000, The Jackson Laboratory, Bay Harbor, ME, USA). These animals were fed a high-fat diet (0.2% total cholesterol, TD 88137, Harlan Teklad, Harlan Laboratories, Madison, WI, USA) for

four months prior to imaging. Four 3-month-old healthy C57BL/6N mice fed with regular chow were used as controls. Four male Sprague-Dawley rats (Central Animal Laboratory, University of Turku, Turku, Finland) were used as the MI model.

All animals were housed under standard conditions in an animal facility, with unrestricted food and water access and 12 hour light cycles with lights on from 6:00 a.m. to 6:00 p.m. All experiments were approved by the Animal Experiment Board in Finland, in addition to the Regional state Administrative Agency for Southern or Eastern Finland. The experiments were carried out according to the European Union directive.

4.11 Statistical Analyses

Values have been represented as mean ± SD with two significant figures. Two-tailed independent samples *t*-tests were used to compare the highest maximum TBR in the aortic arch of atherosclerotic mice and control mice *in vivo*. Two-tailed independent samples *t*-tests were also used to compare the uptake of [^{68}Ga]Ga-NOTA-Folate between atherosclerotic mice and control mice *ex vivo* in various organs, measured using a gamma counter, 120 minutes post-injection. Paired *t*-tests were used to compare the *in vitro* uptake between different tissues from the same subjects on the same ARG imaging plates, with *P* values of less than 0.05 considered significant. All statistical analyses were done using Microsoft Excel.

5 RESULTS

5.1 Radiosynthesis of [^{68}Ga]Ga-NOTA-Folate.

The radiosynthesis of [^{68}Ga]Ga-NOTA-Folate for *in vivo* imaging was successful, as determined by the QC using the HPLC protocol detailed earlier. The results yielded a clear solution with no particles and a radiochemical purity of 99.4 ± 0.56% (n=4). As two mice would be imaged one hour apart for every batch produced, and the maximum radioactivity for the imaging camera was 13 MBq, the product decay was calculated from the end of synthesis to the estimated injection time approximately 10 minutes after. Taking into account the decay and the maximum injection volume being 100 µL for each mouse, the ordered amount for each batch at the end of synthesis was calculated to be 520 MBq/mL, with the desired radioactivity concentration being determined by the last mouse imaged as 330 MBq/mL. The average radioactivity was 328 ± 29 MBq and the radioactivity concentration was 517 ± 45 MBq/mL, adhering closely to the calculated desired amounts. Additionally, the molar activity of 16 ± 1.4 GBq/µmol.

	Desired	**Actual (n = 4)**
Radiochemical Purity	≥95%	99.4 ± 0.56%
Radioactivity Concentration	520 MBq/mL	517 ± 45 MBq/mL
Molar Activity (A_m)	As high as possible	16 ± 1.4 GBq/µL

Table 1. [^{68}Ga]Ga-NOTA-Folate radiosynthesis results.

5.2 Optimization of Concentrated [^{68}Ga]Ga-NOTA-Folate Radiosynthesis Procedure.

After testing NOTA-Folate precursor concentrations of 10 nmol, 7 nmol, and 5 nmol, the highest product purity was determined using iTLC and showed that using 10 nmol of precursor yielded 99 ± 0.26% purity (n=6) the purity. Using 7 nmol of precursor also exceeded the desired ≥95% purity threshold at 98 ± 1.4% purity (n=3). When using 5 nmol

of precursor, the average purity was below the desired amount with 92 ± 1.9% (n=3) purity. When visualizing the QC using iTLC and ARG of [^{68}Ga]Ga-NOTA-Folate, free ^{68}Ga, and both applied to the same strip, the pure [^{68}Ga]Ga-NOTA-Folate remained at the bottom of the strip while the free ^{68}Ga, having bound to the citric acid developer and becoming ^{68}Ga-Citrate, was seen at the top of the strip.

NOTA-Folate Precursor Concentration	Radiochemical Purity
5 nmol*	92 ± 1.9%
7 nmol*	98 ± 1.4%
10 nmol†	99 ± 0.26%

Table 2. Radiochemical purity of [^{68}Ga]Ga-NOTA-Folate using varying NOTA-Folate precursor amounts, calculated by Wizard gamma counter CPS results. *n=3. †n=6.

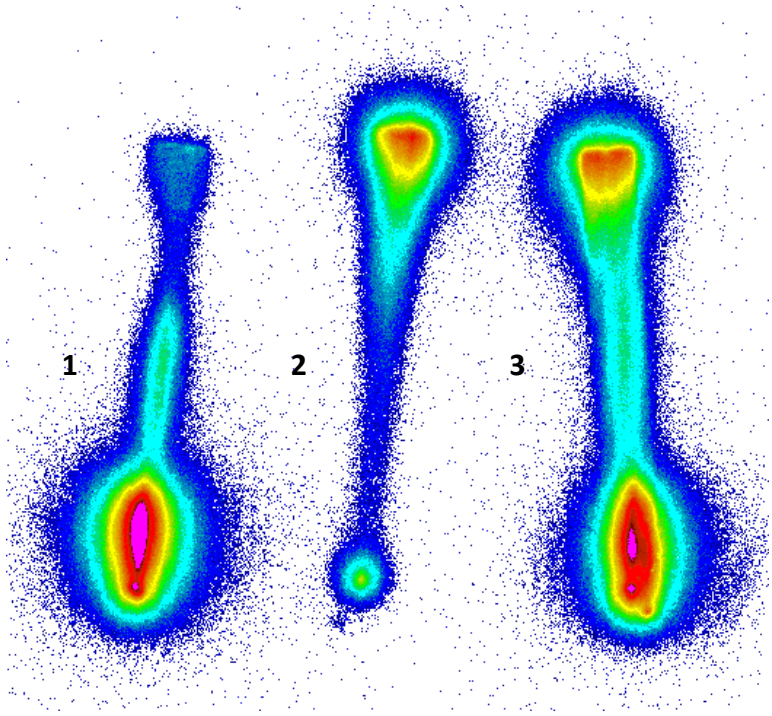

Figure 9. Quality control analysis of concentrated [^{68}Ga]Ga-NOTA-Folate synthesis using 10 nmol of NOTA-Folate using iTLC and ARG; (**1**) [^{68}Ga]Ga-NOTA-Folate end product, (**2**) ^{68}Ga-Citrate, (**3**) [^{68}Ga]Ga-NOTA-Folate and ^{68}Ga-Citrate.

5.3 In Vivo Results.

Upon analysis of the *in vivo* PET/CT scans, the highest maximum TBR in the aortic arch of atherosclerotic mice, measured as SUV, was determined to be 2.6 ± 1.9 (n = 4), which did not show a significant difference from the 1.8 ± 0.046 (n = 4) of the healthy control group (P = 0.50). Additionally, the %ID/g in the aortic arches of atherosclerotic mice was slightly lower than that of the control group at 1.6 ± 0.16 compared to 1.8 ± 0.046, though this difference was not significant (P = 0.11).

The atherosclerotic mice showed higher variances among the SUV and %ID/mL in comparison to the healthy controls, which could be due to the variations in plaque formation among the animals. Upon sacrificing the animals, it was observed that the atherosclerotic mice hardly had visible plaque. This could be attributed to various factors, such as a short time with the high-fat diet, or the fact that some mice may have eaten more than others. The organs with the highest observed accumulation of [^{68}Ga]Ga-NOTA-Folate were the kidneys and the bladder, as seen in Figure 10.

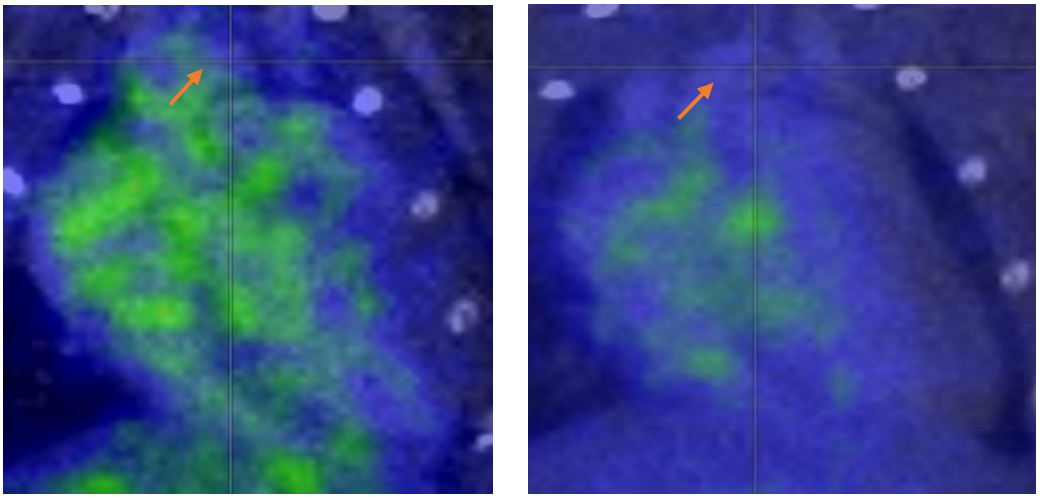

Figure 10. [^{68}Ga]Ga-NOTA-Folate PET/CT images; left represents atherosclerotic mouse, right represents healthy control mouse. Arrows denote the aortic arch.

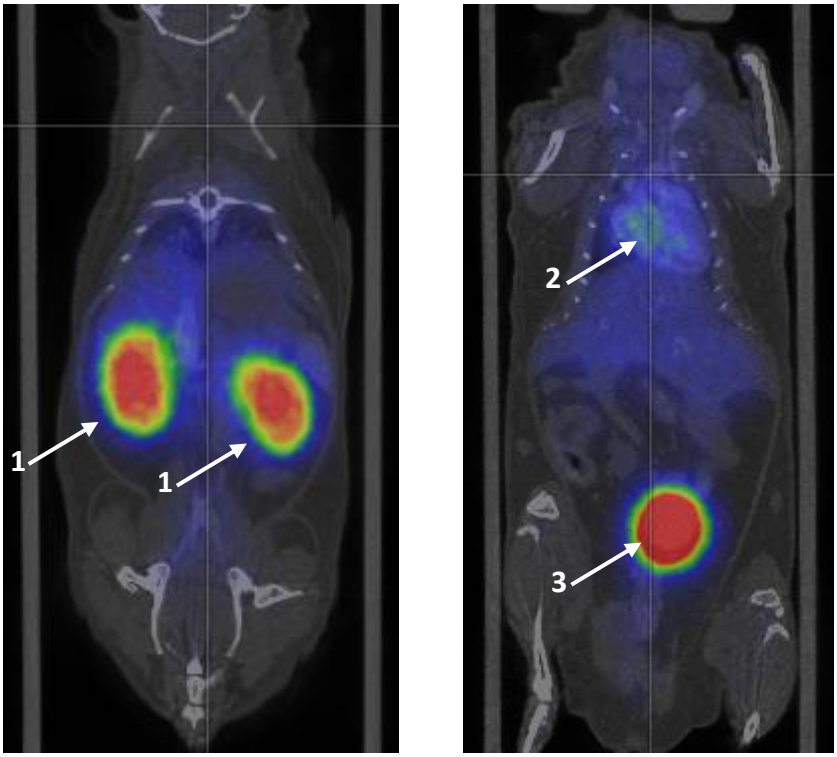

Figure 11. *In vivo* coronal segments showing [^{68}Ga]Ga-NOTA-Folate accumulation the (**1**) kidneys, (**2**) heart, and (**3**) bladder of mice.

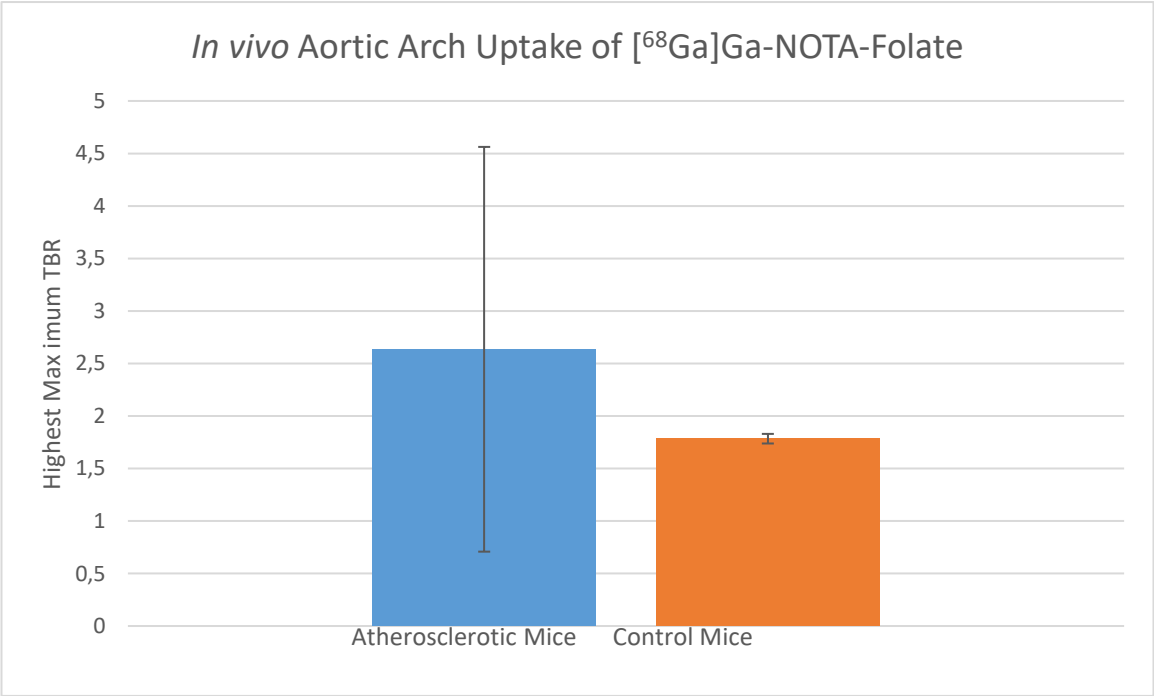

Figure 12. Highest maximum TBR in SUV of the aortic arch calculated between atherosclerotic mice and healthy control mice (P = 0.50, n=4, analyzed using an unpaired t-test).

5.4 Ex Vivo Results.

The aortas of the four atherosclerotic mice were analyzed for [^{68}Ga]Ga-NOTA-Folate binding in the plaques, adventitia and healthy vessel wall. Upon comparing these tissue groups, they were not considered to be significantly different ($P_{plaque,\ wall}$ = 0.057, $P_{plaque,\ adventitia}$ = 0.44, $P_{wall,\ adventitia}$ = 0.18). Additionally, the plaque-to-wall binding ratio was 1.44 ± 0.17. There was high variations among the plaques, which were all averaged to 40 ± 18 PSL/mm^2 (n=4) and the wall tissues, which was 28 ± 13 PSL/mm^2 (n=4).

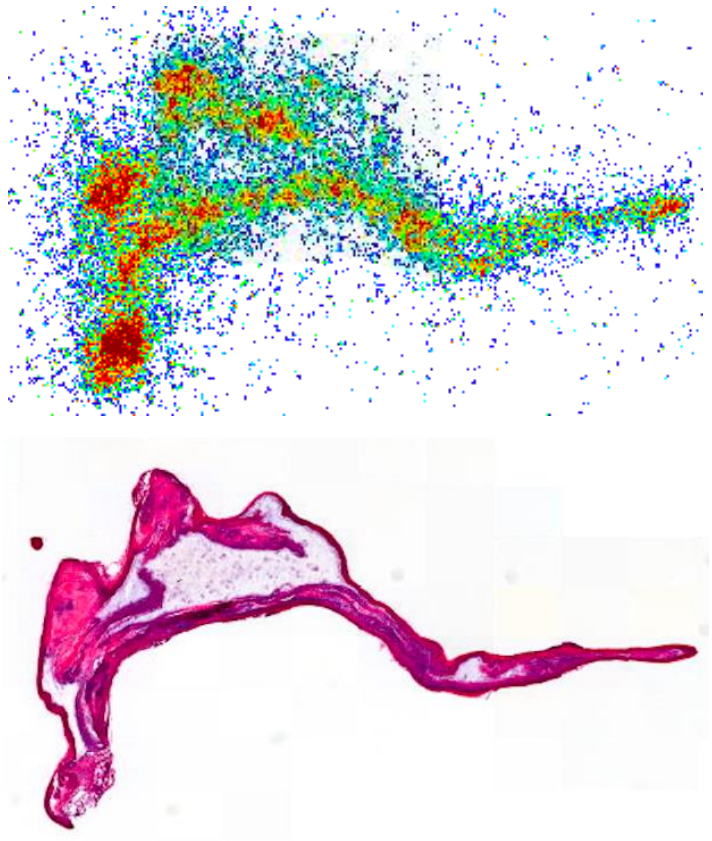

Figure 13. Ex vivo binding of [^{68}Ga]Ga-NOTA-Folate in atherosclerotic mouse aorta. Top represents autoradiograph of the aorta cryosection. Bottom represents the same tissue section stained with H&E for histological reference.

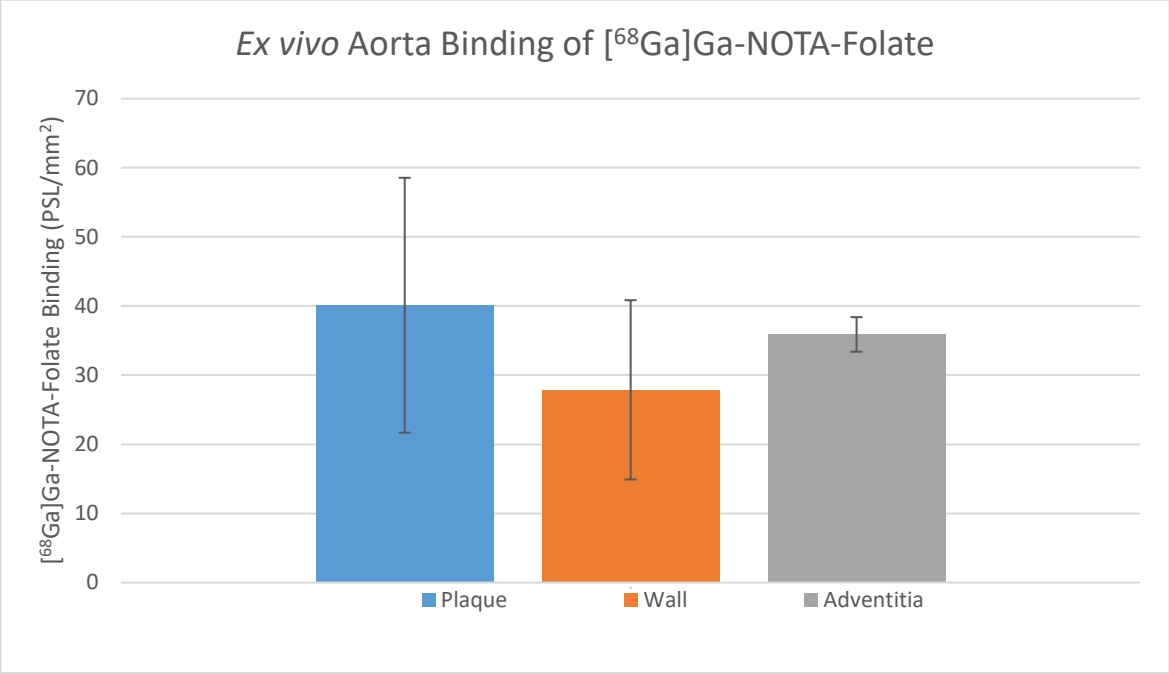

Figure 14. The binding of [^{68}Ga]Ga-NOTA-Folate to plaque, wall and adventitia tissues in atherosclerotic mouse aortas *ex vivo* (mean ± SD, n=4, analyzed using a paired *t*-test).

The biodistribution of [^{68}Ga]Ga-NOTA-Folate was assessed by *ex vivo* gamma counting. The results showed no significant differences in uptake of [^{68}Ga]Ga-NOTA-Folate between most organs of the atherosclerotic mice and the healthy control mice; only the hearts (P = 0.024) and stomachs (P = 0.0074) of the atherosclerotic mice showed significantly higher uptake when compared to the healthy controls. Additionally, the lymph nodes of the control mice had significantly higher uptake than that of the atherosclerotic mice (P = 0.03). The highest uptake was seen in the kidneys, with an average of around 25 ± 6.8 %ID/g in atherosclerotic mice and 26 ± 3.4 %ID/g.

Tissue	**LDLR$^{-/-}$ ApoB$^{100/100}$ atherosclerotic mice (n=4)**	**C57BL/6N control mice (n=4)**	***P* Value**
Aorta	0.93 ± 0.34	0.48 ± 0.33	P = 0.11
Muscle	0.19 ± 0.051	0.21 ± 0.023	P = 0.67
Blood	0.24 ± 0.044	0.22 ± 0.032	P = 0.39
Plasma	0.43 ± 0.13	0.35 ± 0.091	P = 0.36

Heart	0.24 ± 0.035	0.17 ± 0.031	$P = 0.024$
Lungs	0.60 ± 0.29*	0.37 ± 0.099	$P = 0.32$
Thymus	0.82 ± 0.86*	0.29 ± 0.12	$P = 0.40$
Liver	0.72 ± 0.21	0.50 ± 0.13	$P = 0.14$
Spleen	0.12 ± 0.0087	0.12 ± 0.032	$P = 0.93$
Pancreas	0.38 ± 0.11	0.30 ± 0.029	$P = 0.28$
Kidneys	25 ± 6.8	26 ± 3.4	$P = 0.79$
Stomach	0.83 ± 0.15	0.43 ± 0.055	$P = 0.0074$
Small intestine	0.51 ± 0.22	0.52 ± 0.20	$P = 0.95$
Large intestine	0.75 ± 0.16	0.51 ± 0.070	$P = 0.054$
Lymph nodes	1.6 ± 0.62	3.3 ± 0.95	$P = 0.030$
WAT	0.26 ± 0.11	0.18 ± 0.025	$P = 0.28$
BAT	0.28 ± 0.18	0.18 ± 0.034	$P = 0.34$
Bone	0.15 ± 0.060	0.10 ± 0.0094	$P = 0.22$
Brain	0.085 ± 0.014	0.072 ± 0.013	$P = 0.23$
Femur	0.15 ± 0.057	0.10 ± 0.024	$P = 0.23$

Table 3. *Ex vivo* biodistribution of [^{68}Ga]Ga-NOTA-Folate in mice 120 minutes after injection, with results expressed as percent of injected radioactivity dose per gram of tissue (%ID/g) (mean ± SD, rounded to two significant figures). *P*-values listed for differences between LDLR$^{-/-}$ ApoB$^{100/100}$ atherosclerotic mice and C57BL/6N control mice analyzed by independent sample *t*-test ($P = 0.05$). *n=3. WAT = white adipose tissue; BAT = brown adipose tissue.

5.5 Metabolite Analyses.

The *in vitro* metabolite analysis (n=1) served to determine what tracer standard to use as well as the HPLC gradient for the remainder of the metabolite analyses. Following *in vivo* imaging, the plasma of the mice was analyzed for metabolites present. This was analyzed using HPLC to compare a tracer standard with no plasma to the plasma of the mice. The

results from the HPLC graphs are shown in Figure 16. When compared to the tracer standard, one major peak was observed close to the intact tracer.

Following this, a plasma protein binding test was done to determine how much [^{68}Ga]Ga-NOTA-Folate could have bound to the plasma proteins. This was done by calculating the ratio of radioactivity in the supernatant liquid from the plasma to that of the pellet. Atherosclerotic mice had an average ratio of 3.8 ± 0.32 (n=4), while the control mice had an average of 4.7 ± 0.67 (n=4). There was no statistically significant difference between the two (P = 0.064).

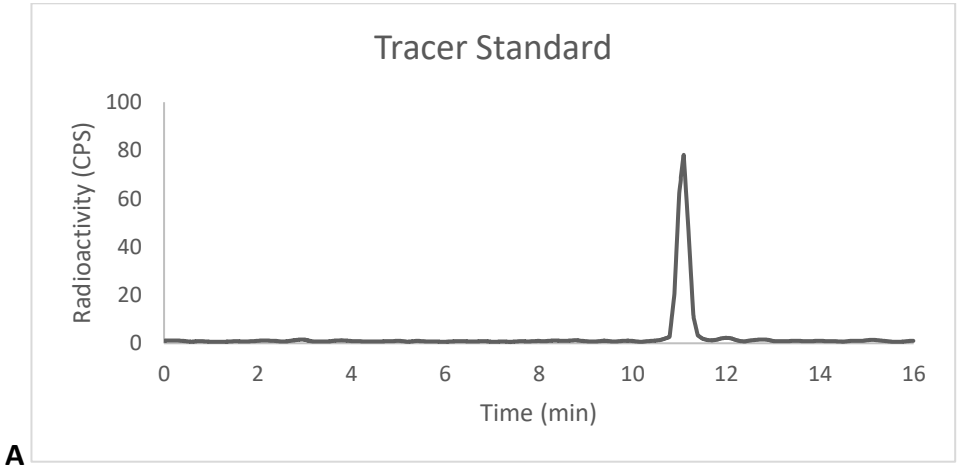

A

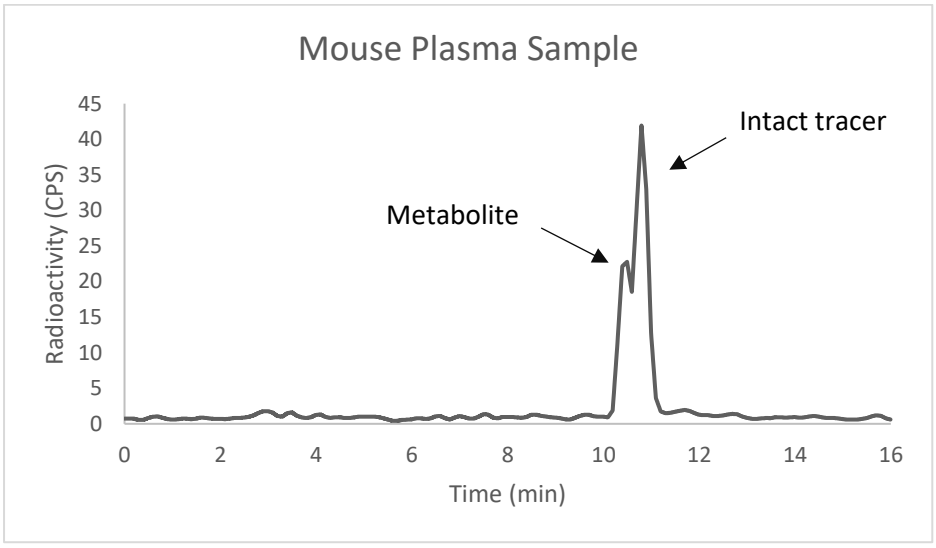

B

Figure 16. Representative radio-HPLC chromatograms of (A) standard [^{68}Ga]Ga-NOTA-Folate in acetonitrile and TFA buffer and (B) a mouse plasma sample.

5.6 In vitro binding in human tissues.

There was significantly higher binding of [^{68}Ga]Ga-NOTA-Folate to atherosclerotic plaque in human carotid artery tissues incubated in only [^{68}Ga]Ga-NOTA-Folate than those tissues incubated with the added blocker (P = 0.013, n=8), showing [^{68}Ga]Ga-NOTA-Folate's specificity to bind to FRs. The same result was observed when comparing the binding to the healthy wall tissue, with the binding being higher in the total binding tissues (P = 0.028, n=7). Furthermore, the ratio of binding in plaque to binding in healthy wall tissue averaged 4.7 ± 4.5 in total binding tissues, while that of blocked tissues averaged 1.4 ± 0.13. Even with the variance in the total binding tissues, the difference in them was still significant (P = 0.018, n=7).

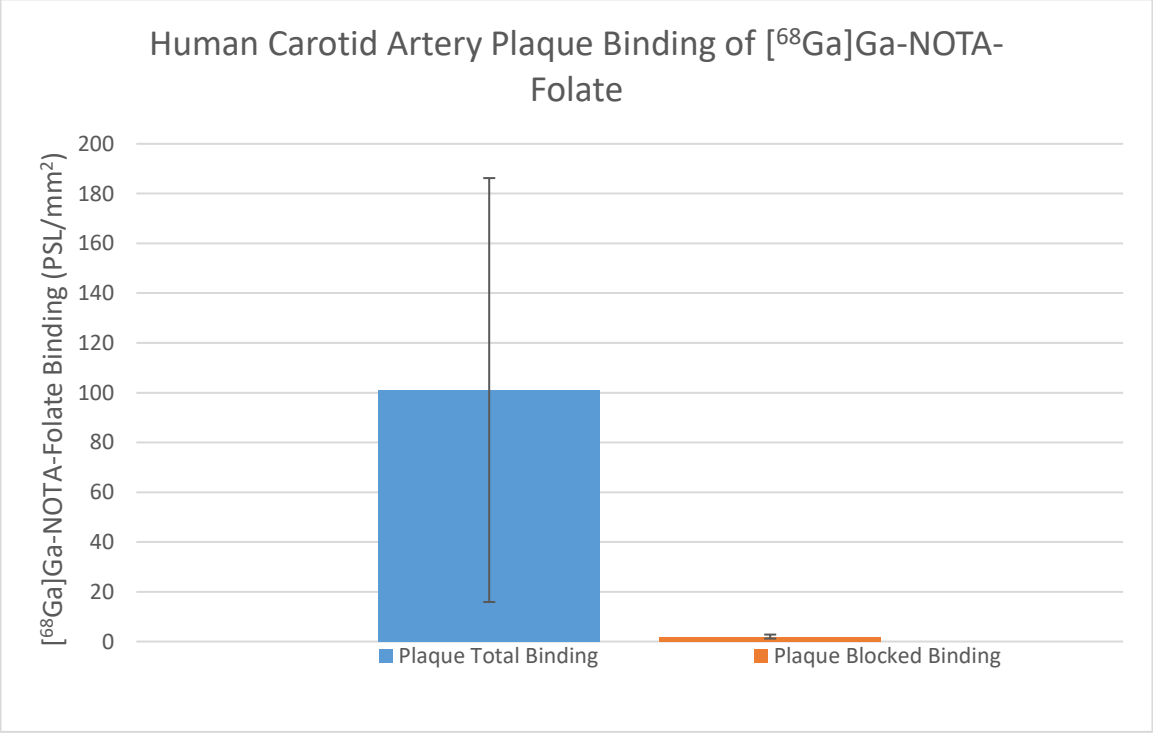

Figure 17. Binding of [^{68}Ga]Ga-NOTA-Folate to plaque in human carotid arteries with and without FR blocker (mean ± SD, P = 0.013, n=8, analyzed using a paired t-test).

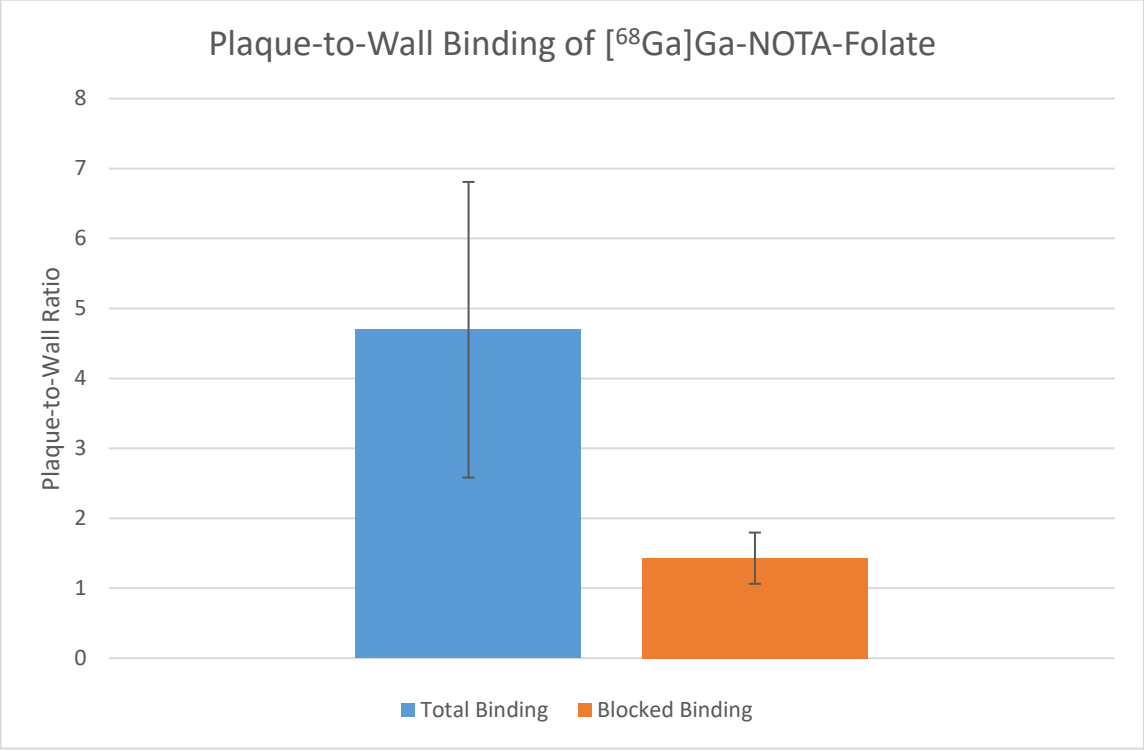

Figure 18. Ratio of [^{68}Ga]Ga-NOTA-Folate binding between atherosclerotic plaques and healthy wall tissue in human carotid arteries with and without FR blocker (mean ± SD, $P = 0.018$, n=7, analyzed using a paired *t*-test).

5.7 MI in vitro *binding.*

[^{68}Ga]Ga-NOTA-Folate proved to bind specifically to FRs when assessed in post-MI inflamed heart tissues with and without folate glucosamine to block the FRs. Binding of [^{68}Ga]Ga-NOTA-Folate was expressed in PSL/mm^2 values, with an average value of 290 ± 10 PSL/mm^2 in MI scar tissues without blocker. By contrast, the tissues treated with 500 times more blocker than tracer had 1.6 ± 0.37 PSL/mm^2 in the MI scar tissues ($P = 0.0021$, n=4).

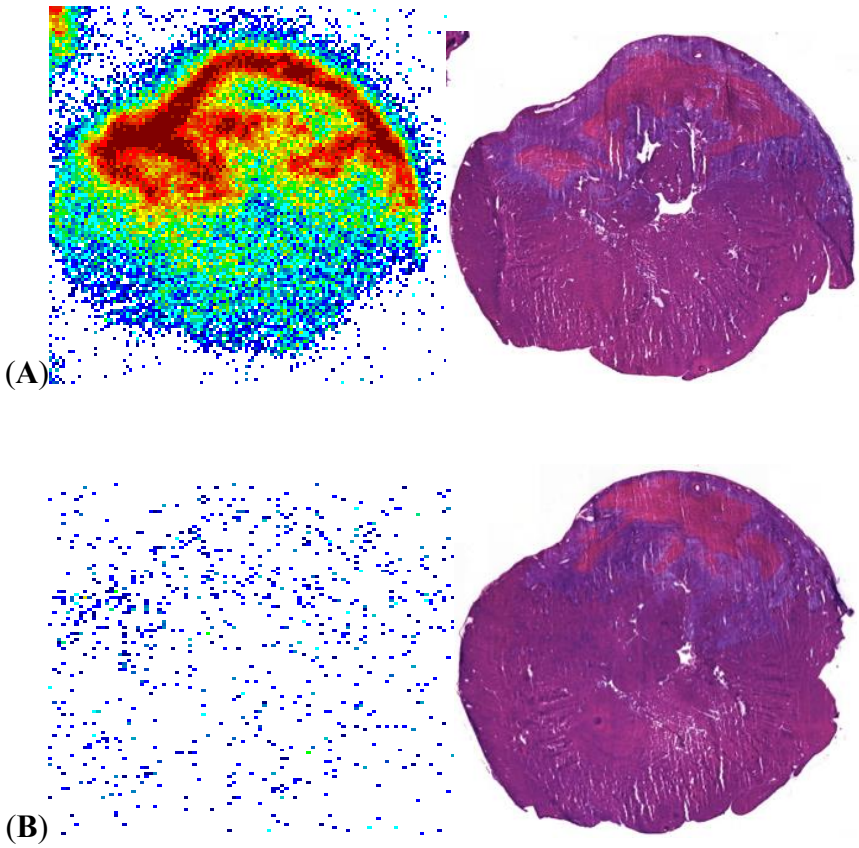

Figure 19. Digital autoradiographs showing binding of [^{68}Ga]Ga-NOTA-Folate with (**A**) no FR blocker and (**B**) with FR blocker in rat hearts 3 days post-MI alongside the same tissues stained with H&E for histological reference.

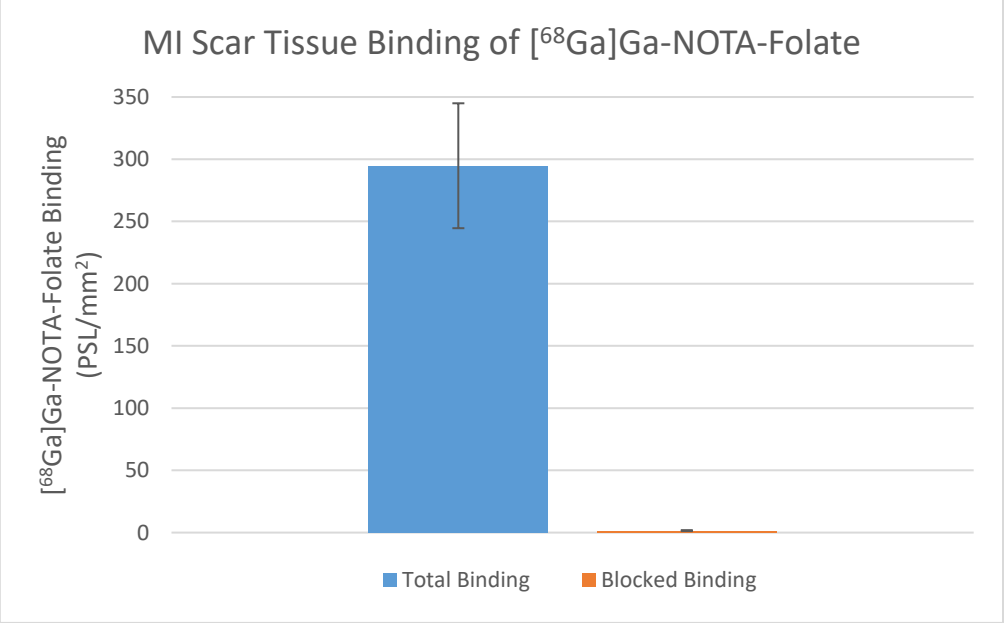

Figure 20. Binding of [^{68}Ga]Ga-NOTA-Folate to MI scar tissue in rat hearts with and without FR blocker (mean ± SD, $P = 0.0021$, n=4, analyzed using a paired *t*-test).

When comparing uptake of [^{68}Ga]Ga-NOTA-Folate in MI scar tissue to the remote healthy tissue, the ratio of the total binding tissues was significantly higher at 5.2 ± 0.83 PSL/mm^2 than that of the blocked tissues was 1.9 ± 0.52 PSL/mm^2 (P = 0.0034, n=4).

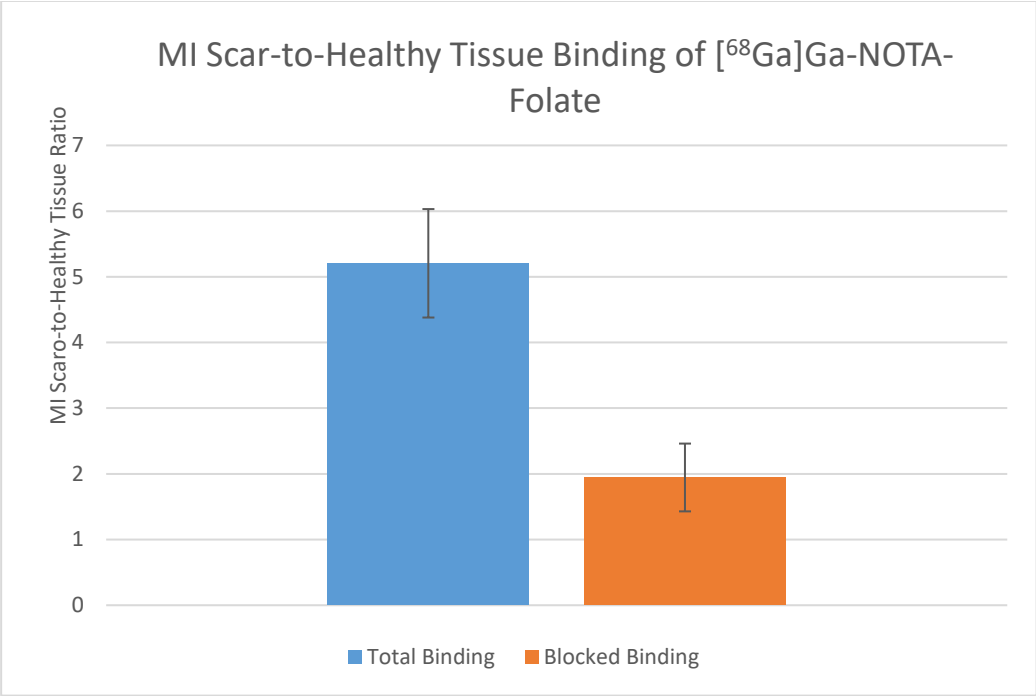

Figure 21. Ratio of [^{68}Ga]Ga-NOTA-Folate binding between MI scar tissue and remote healthy tissue in rat hearts with and without FR blocker (mean ± SD, P = 0.0034, n=4,analyzed using a paired t-test).

Uptake in the remote healthy tissues was also significantly different among the two groups, with the total binding tissues averaging 57 ± 30 PSL/mm^2 and the blocked tissues averaging 0.90 ± 0.52 PSL/mm^2 (P = 0.00025, n=4).

5 DISCUSSION

While atherosclerosis can be largely prevented by leading a healthy lifestyle and making proper dietary choices, many consider this to be too much work and instead adhere to Western-type diets. Given that cardiovascular disease is the leading cause of death in developed countries affecting millions worldwide, along with the fact that atherosclerosis usually goes undetected until MI, stroke, or blood clots occur, there is an urgent need for non-invasive diagnosing and disease monitoring. Pre-clinical imaging is a key milestone towards achieving this goal, as it is unethical to test newly developed radiotracers directly in humans and expose them not only to the radiation, but any potential unknown side effects.

Studies done *in vitro* help to understand whether a radiotracer will bind to tissues, though this cannot account for the numerous biological processes that may affect it in a living organism. Pre-clinical imaging gives an essential understanding of how a radiotracer may behave once in a biological system, where a multitude of factors can impact its ability to bind to the targeted tissues. While mice and humans differ in many ways, the mouse model used allowed for plaque to be imaged with some basic understandings of where else a radiotracer may accumulate. These understandings are crucial in determining whether a radiotracer is a potentially suitable tracer for clinical imaging of atherosclerosis or MI healing.

The novel radiotracer [^{68}Ga]Ga-NOTA-Folate was synthesized successfully and while it did not appear to bind to plaques in the aortic arches of atherosclerotic mice *in vivo,* [^{68}Ga]Ga-NOTA-Folate did show specific binding to FRs *in vitro* to plaques in human carotid arteries and rat MI scar tissue. While more experiments are needed to confirm the results *in vivo*, the *in vitro* blocked binding experiments supported the hypothesis that attaching a radionuclide to the folate molecule lead to specific binding of the molecule to the FRs present in the macrophages.

The radiosynthesis of [^{68}Ga]Ga-NOTA-Folate gave a great result. As the method had been done previously, the hypothesis of obtaining a successful end product with high purity, yield and molar activity was supported. The overall synthesis took around 20 minutes from start

of elution to measuring the radioactivity of the end product and was conveniently done in a radiochemistry lab within the confines of a hot cell.

When optimizing the protocol for synthesizing concentrated [^{68}Ga]Ga-NOTA-Folate, the various precursor concentrations used showed that while adding 10 nmol a very high purity of 99% can be obtained, only 7 nmol of NOTA-Folate were necessary to achieve the desired purity of ≥95%. By using 7 nmol instead of 10 nmol, 6 μL of precursor may be saved per synthesis while still ending with a highly pure end product. While the ARG of iTLC is not necessary for QC if a gamma counter is available, the results showed clear separation of the desired [^{68}Ga]Ga-NOTA-Folate to that of the free ^{68}Ga. This occurred because the free ^{68}Ga bound to the citric acid developer, forming ^{68}Ga-Citrate. ^{68}Ga-Citrate is both smaller and more polar than [^{68}Ga]Ga-NOTA-Folate, therefore any free ^{68}Ga impurities can be separated and detected using iTLC with citric acid as the developer. If iTLC strips are not available, another method for analyzing the QC of the end product would be by using HPLC, as was done with the *in vivo* and *in vitro* experiments. While the QC with HPLC does take 15 minutes to the 1 minute of gamma counting per full iTLC strip, it serves as a great way to verify and visualize the product purity.

While the protocol used for the radiosynthesis of [^{68}Ga]Ga-NOTA-Folate for *in vivo* and *ex vivo* experiments met each goal, it may be worthwhile to see if there is room for optimization, as there was in the concentrated [^{68}Ga]Ga-NOTA-Folate radiosynthesis. Given the results from the concentrated radiosynthesis, where high purity of ≥95% met while using 7 nmol of NOTA-Folate precursor, the question is raised as to whether less amounts of NOTA-Folate precursor can be used in the first [^{68}Ga]Ga-NOTA-Folate radiosynthesis protocol, as this could perhaps be useful for a more efficient use of the precursor.

There was no significant difference in the *in vivo* uptake of [^{68}Ga]Ga-NOTA-Folate to the aortic arch of the atherosclerotic mice when compared to that of the healthy controls. Additionally, there was high variation in the uptake among the atherosclerotic mice. While it is possible that [^{68}Ga]Ga-NOTA-Folate may not be the most optimal tracer to image atherosclerotic plaques, the specific binding experiments proving that [^{68}Ga]Ga-NOTA-

Folate does bind specifically to FRs led to the expectation and hope that the *in vivo* results would show some significant difference within the groups. Previous experiments aimed at assessing a tracer's ability to target atherosclerotic inflammation have used the same experimental mouse model with the same age, gender, and time fed the high-fat diet and, while this cannot be validated, the amount of plaque observed during harvesting in the aortic arches of the atherosclerotic mice was noticeably less than in previous experiments.

Limitations in the *in vivo* experiments could be due to the sample size in the being too small. As each mouse has its own metabolism that causes plaque development at various rates, having more atherosclerotic mice could potentially decrease the variation among results. Additionally, as the mice were fed without restrictions, there was no way to know how much food each mouse ate. Being that atherosclerosis is a nutrition-related disease, this could cause some variation, as some mice may not have eaten as much as others and this could have potentially impacted the degree of plaque formation. Another limitation was using male mice, therefore it remains unclear if females may metabolize [^{68}Ga]Ga-NOTA-Folate differently. Furthermore, while the ROIs were drawn carefully to avoid including outside areas, it is also possible that unintentional human error could have caused some unintentional variability. Due to these limitations, further experiments should done to try and decrease the observed variation before arriving to a definite conclusion. Additionally, the time given the high-fat diet could be extended in future experiments to help increase the chances of developing more atherosclerotic plaques.

The *ex vivo* aortas from the imaged atherosclerotic mice showed no significant difference in [^{68}Ga]Ga-NOTA-Folate binding among the different tissues present. The plaque-to-wall ratio showed that [^{68}Ga]Ga-NOTA-Folate was around 1.4 times more likely to bind to plaques than the wall. As the *in vivo* results showed no difference with high variations in aortic arch uptake and there was little observed plaque when harvesting the aorta, further investigation should be done before arriving to a definitive conclusion on whether or not [^{68}Ga]Ga-NOTA-Folate is a suitable tracer for imaging atherosclerotic plaques.

Ex vivo gamma counting showed higher %ID/g in the hearts of atherosclerotic mice than those of the healthy control mice. Additionally, the *ex vivo* gamma counting showed the highest uptake of [^{68}Ga]Ga-NOTA-Folate to be in the kidneys with nearly a quarter of the %ID/g being found in the kidneys of both experimental groups. This is not surprising, as one of the most common limitations with radiotracers is their high uptake in the highly metabolically active kidney, contributing to background radiation in the area of interest. While they were not available for the *ex vivo* gamma counting, the bladders showed high uptake in the PET/CT images, which was expected as the kidneys excrete toxins via the bladder. As the target for imaging was the aortic arch, this high uptake in the kidneys and bladder did not contribute greatly to the observed signal of the aortic arch.

Additionally, while it may not have been as high as the kidneys or bladder, the heart had higher uptake than most other organs. Among the two groups, uptake of [^{68}Ga]Ga-NOTA-Folate in the heart was notably higher among the atherosclerotic mice than the controls. The exact cause can only be speculated at this point, however one theory may be that as the atherosclerotic mice are genetically predisposed to developing more plaque than the healthy controls, it is possible that there could have been more plaque among other arteries in the heart to which [^{68}Ga]Ga-NOTA-Folate may have bound. Due once more to the high variability in the results, more experiments should need to be done to verify whether there is truly more accumulation of [^{68}Ga]Ga-NOTA-Folate in the hearts of the atherosclerotic mice with some quantifying methods, such as *ex vivo* ARG, to further support the findings. While the uptake of [^{68}Ga]Ga-NOTA-Folate was significantly less than the kidneys and bladder, the uptake in the heart could have potentially contributed to some minimal background noise in the aortic arch, given their proximity to one another.

Furthermore, a difference in the uptake of [^{68}Ga]Ga-NOTA-Folate in the stomach was observed between the two different groups, as the atherosclerotic mice had significantly higher uptake than the healthy controls. At this point it is not known why this is, however one theory could be that plaque could have built up in the stomach aorta. This theory would need to be verified perhaps with *ex vivo* digital ARG if possible.

The uptake of [^{68}Ga]Ga-NOTA-Folate was higher in the control mice in comparison to the atherosclerotic mice. It is not currently known why this may have occurred, or if this has been seen in previous experiments between atherosclerotic mice and control mice of the same strains. This finding raises awareness to retrospectively assess previous experiments and quantify any potential differences found in order to determine why this difference in uptake may occur. Additionally, one metabolite was found when analyzing the *ex vivo* plasma of the mice. The identity of this metabolite is not known, nor is its ability to cross or impact tissues.

The blocked binding experiments done *in vitro* demonstrated that [^{68}Ga]Ga-NOTA-Folate does indeed bind specifically to FRs, a finding supported in two different tissues and species *in vitro.* Not only was the binding of [^{68}Ga]Ga-NOTA-Folate significantly different among the unblocked and blocked plaques, but in the total binding human carotid artery samples, the average plaque-to-wall ratio proved that [^{68}Ga]Ga-NOTA-Folate was binding almost five times higher to the plaque than the healthy vessel wall. Similarly, the post-MI rat hearts showed around five times more binding to the MI scar tissue than that of the remote healthy tissue.

Due to the extent of plaque in the human carotid arteries, some of the samples had ruptured calcified plaque upon cryosectioning, causing overlap of the tissues. This reduced the number of clear ROIs among the tissues. While there were still enough areas available to make several ROIs per sample, the damage from the rupture limited the total collection of data. In future experiments, as the extent of plaques and calcifications cannot be controlled, perhaps some notice of this sensibility causing potential problems may be considered when cryosectioning to avoid further damages to the tissues. Additionally, regarding the MI healing tissues, only male rat heart sections were used, again echoing the limitation that there could be unknown metabolic differences among the genders impacting the healing after MI.

In order to determine whether [^{68}Ga]Ga-NOTA-Folate is suitable for targeting the FRs present in active macrophages, high concentrations of folate glucosamine blocker are needed to verify the binding specificity of the radiotracer. However, there may be many other factors

that impact [^{68}Ga]Ga-NOTA-Folate binding once in the body. This can mean that while some [^{68}Ga]Ga-NOTA-Folate may bind to FRs, it is possible for some other molecule or biological process to block the binding of [^{68}Ga]Ga-NOTA-Folate *in vivo*. To clarify this doubt, [^{68}Ga]Ga-NOTA-Folate needs to be studied *in vivo* and while this has already been preliminarily done in atherosclerotic mice, it will need to be done in MI-healing rats to verify the specific binding ability to the MI scar tissue.

The next step in assessing the effectiveness of [^{68}Ga]Ga-NOTA-Folate as a radiotracer would be to perform more experiments using more animals to decrease variability and feeding the high-fat diet for a longer period to give a higher chance for more plaque to develop, and if results show specific uptake to atherosclerotic plaques *in vivo*, [^{68}Ga]Ga-NOTA-Folate should be compared with [^{18}F]-FDG to compare their biodistribution. Additionally, *in vivo* experiments should be done to observe whether there is uptake of [^{68}Ga]Ga-NOTA-Folate in inflamed scar tissue of rats at set timepoints after having undergone MI operation.

6 CONCLUSION

Molecular imaging is a fast-growing technique that has the potential to provide a means to visualize disease diagnosis, monitoring, and potential treatment options. By studying the novel radiotracer [^{68}Ga]Ga-NOTA-Folate pre-clinically, essential information is gained to determine whether it is a suitable radiotracer to image inflammation due to atherosclerosis and MI healing.

[^{68}Ga]Ga-NOTA-Folate was shown to bind specifically to FRs, indicating that it has potential to molecularly image inflammation due to atherosclerotic plaques and healing after MI. More PET/CT *in vivo* imaging experiments should be done to verify its ability to image to atherosclerotic plaques due to the high variability observed. [^{68}Ga]Ga-NOTA-Folate uptake is high in the kidneys and bladder and one metabolite was observed in the plasma, which remains to be identified. As [^{68}Ga]Ga-NOTA-Folate showed significant binding to post-MI scar tissue in rats relative to the remote healthy tissue, it seems promising for molecular imaging of MI healing and therefore should be assessed *in vivo* to determine its effectiveness in a biological system.

7 ACKNOWLEDGEMENTS

I would like to give the sincerest thank you to my supervisors, Anne Roivainen, Xiang-Guo Li, and Antti Saraste for allowing me to work and learn in their great lab group. I would also like to give many thanks to my colleagues in the group, which have all been readily available, immensely helpful, and kind: Arghavan Jahandideh, Heidi Liljenbäck, Helena Virtanen, Aake Petteri Honkaniemi, Imran Iqbal, Jenni Virta, Maria Grönam, Maxwell Miner, Mia Ståhle, Olli Moisio, Petri Elo, Putri Andriana, Päivi Marjamäki, Riikka Viitanen, and Senthil Palani.

My sincerest of gratitude to Xiang and Olli for helping with the radiochemistry as well as with my thesis: Xiang has provided the image for Figure 3 and Olli has let me integrate his results for the concentrated [^{68}Ga]Ga-NOTA-Folate synthesis, with data from the 5 and 7 nmol tests, along with three experiments for 10 nmol tests. Additionally, I would like to thank Päivi for helping with the *in vitro* binding experiments, as well as Jenni, Riikka, Mia, Senthil, and Max for help with the image analysis process. Furthermore, thank you to Heidi, Aake, and Jenni for the vital assistance during the *in vivo* experiments.

I would also like to thank the BIMA staff for always being available and helpful during my studies. *Kiitos* to the University of Turku and the PET Centre whose resources have allowed me to complete this work, supported by my competent and endearing professors and peers.

While my infinite gratitude cannot be put into words, I would like to give an immense thank you to my support system; my parents William and Noemi, my sister Barbara, my tía Luly, my abuelita Noemy, my boyfriend Tomi and his welcoming family, and my friends Tina, Jamie, Dora, Oona, Dado, Tzu-Chen and Andriana. Thank you for always being there when I have needed it.

Because one time is not enough, a special thank you to my father William, without whom I would not have been able to go on this adventure that has been moving to Finland to complete this program.

8 REFERENCES

Achenbach, S., Moselewski, F., Ropers, D., Ferencik, M., Hoffmann, U., MacNeill, B., Pohle, K., Baum, U., Anders, K., Jang, I. et al. 2004. Detection of Calcified and Noncalcified Coronary Atherosclerotic Plaque by Contrast-Enhanced, Submillimeter Spiral Computed Tomography. *Circ.* 109:14-17.

Aljammaz I., B. Al-Otaibi, N. Al-Hokbany, S. Amer, and S. Okarvi. 2014. Development and Pre-clinical Evaluation of New ^{68}Ga-NOTA-folate Conjugates for PET Imaging of Folate Receptor-positive Tumors. *Anticancer Res*. 34:6547-6556.

Al-Mamari, A. 2009. Atherosclerosis and Physical Activity. *Oman Med J.* 24:173-178.

Baccarelli, A. and Benjamin, E. J. 2013. Triggers of Myocardial Infarction for the Individual and in the Community. *Lancet.* 377:694-696.

Barthe, N., Maîtrejean, S., and Cardona, A. 2012. High-Resolution Beta Imaging. In: *Handbook of Radioactivity Analysis,* pp.1209-1242. Elsevier, Amsterdam.

Bélanger, J. M. R., Paré, J. R. J., and Sigouin, M. 1997. High Performance Liquid Chromatography (HPLC): Principles and Applications. In: *Instrumental Methods in Food Analysis,* pp. 37-59. Elsevier, Amsterdam.

Bele, A. A., and Khale, A. 2011. An Overview on Thin Layer Chromatography. *Int. J Pharm Sci Rev Res.* 2:256-267.

Bentzon, J. F., F. Otsuka, R. Virmani, and E. Falk. 2014. Mechanisms of Plaque Formation and Turpture. *Circ Res*. 114:1852-1866.

Bergheanu, S. C., Bodde, M. C., and Jukema J. W. 2017. Pathophysiology and treatment of atherosclerosis. *Neth Heart J.* 25:231-242.

Bolus, N. E. 2001. Basic Review of Radiation Biology and Terminology. *J Nucl Med Technol.* 29:67-73.

Brand, C., V. A. Longo, M. Groaning, W. A. Weber, and T. Reier. 2017. Development of a New Folate-Derived Ga-68-Based PET Imaging Agent. *Mol Imaging Biol*. 19:754-761.

Brechbiel, M. W. Bifunctional Chelates for Metal Nuclides. *Q J Nucl Med Mol Imaging*. 52:166-173.

Chen, K. and Chen, X. 2010. Design and Development of Molecular Imaging Probes. *Curr Top Med Chem.* 10:1227-1236.

Chen, W. and Dilsizian, V. 2015. PET Assessment of Vascular Inflammation and Atherosclerotic Plaques: SUV or TBR? *J Nucl Med.* 56:503-504.

Chin, B. B., Nakamoto, T., Kraitchman, D., Marshall, L. and Wahl, R. 2003. PET-CT Evaluation of 2-Deoxy-2-[^{18}F]-Fluoro-D-Glucose Myocardial Uptake: Effect of Respiratory Motion. *Mol Imaging Biol.* 5:57-64.

Clifton, P. and Keogh, J. Cholesterol-Lowering Effects of Plant Sterols in One Serve of Wholegrain Wheat Breakfast Cereal Biscuits—A Randomized Crossover Clinical Trial. *Foods.* 7:39.

Crowley, T. E. 2020. High-performance liquid chromatography. In: *Purification and Characterization of Secondary Metabolites*, pp. 49-58. Elsevier, Amsterdam.

Curley, D., B. L. Plaza, A. M. Shah, and R. M. Botnar. 2018. Molecular imaging of cardiac remodeling after myocardial infarction. *Basic Res Cardiol*. 113:10.

D'Ambrosio, D., Zagni, F., Spinelli, A. E. and Marengo, M. 2013. Attenuation Correction for Small Animal PET Images: A Comparison of Two Methods. *Comput Math Method M.* 2013. doi: 10.1155/2013/103476.

de Groot, E., van Leuven, S. I., Duivenvoorden, R., Meuwese, M. C., Akdim, F., Bots, M. L., and Kastelein, J. J. P. 2008. Measurement of carotid intima-media thickness to assess progression and regression of atherosclerosis. *Nat Rev Cardiol.* 5:280-288.

De Oliveira, I. M., Martins, P. A., da Silva, J. L., Ramos, M. P. S., Lima, J. A. S., Pujatti, P. B., Fukumori, N. T. O., and Matsuda, M. M. N. 2011. Alternative Methods for Radiochemical Purity Testing in Radiopharmaceuticals. *International Nuclear Atlantic Conference.* ISBN: 978-85-99141-04-5.

Decristoforo, C., Zolle, I., Rakáis, F., Imre, J., Jánoki, G., and Hesselwood, S. R. 2007. Quality Control Methods of ^{99m}Tc Pharmaceuticals In: *Technetium-99m Pharmaceuticals,* pp. 123-150. Springer, Berlin.

Doucette, M., and V. L. Stevens. 2001. Folate receptor Function Is Regulated in Response to Different Cellular Growth Rates in Cultured Mammalian Cells. *J Nut.* 131:2819-2825.

Esmaeilzadeh, M., Parsaee, M., and Maleki, M. 2013. The Role of Echocardiography in Coronary Artery Disease and Acute Myocardial Infarction. *J Tehran Heart Cent.* 8:1-13.

Ford, E. S., Ajani, U. A., Croft, J. B., Critchley, J. A., Labarthe, D. R., Kottke, T. E., Giles, W. H., and Capewell, S. 2007. Explaining the Decreast in U.S. Deaths from Coronary Disease, 1980-2000. *N Engl J Med.* 356:2388-2398.

Howard-Alpe, G. M., Sear, J. W., and Foex, P. 2006. Methods of detecting atherosclerosis in non-cardiac surgical patients; the role of biochemical markers.

Huang, B., Law, M. W., and Khong, P. 2009. Whole-Body PET/CT Scanning: Estimation of Radiation Dose and Cancer Risk. *Radiol.* 251:166-174.

Hyafil, F., and J. Vigne. 2019. Imaging inflammation in atherosclerotic plaques: Just make it easy! *J Nucl Cardiol*. 26:1705-1708.

Ibañez, B., Badimon, J. J., and Garcia, M. J. 2009. Diagnosis of Atherosclerosis by Imaging. *Am J Med.* 122:S15-S25.

ICRP. 2007. The 2007 Recommendations of the International Commission on Radiological Protection. *ICRP Publication 103*, Ann. ICRP 37.

Ismahil, M. A., Hamid, T., Basnal, S. S., Patel, B., Kingery, J. R., and Prabhu, S. D. 2014. Remodeling of the mononuclear phagocyte network underlies chronic inflammation and disease progression in heart failure: critical importance of the cardiosplenic axis. *Circ Res.* 114:266-282.

Jager, N. A., N. Teteloshvili, C. J. Zeebregts, J. Westra, and M. Bijl. 2012. Macrophage folate receptor-B (FR-β) expression in auto-immune inflammatory rheumatic diseases: A forthcoming marker for cardiovascular risk? *Autoimmun Rev*. 11:621-626.

Kiugel, M., I. Dijkgraaf, V. Kytö, S. Helin, H. Liljenbäck, T. Saanijoki, C. Yim, V. Oikonen, P. Saukko, J. Knuuti et al. 2014. Dimeric [^{68}Ga]DOTA-RDG Peptide Targeting $\alpha_v\beta_3$ Integrin Reveals Exracellular Matrix Alterations after Myocardial Infarction. *Mol Imaging Biol*. 16:793-801.

Kochanek, K. D., Murphy, S. L., Xu, J., and Arias, E. 2019. Deaths: Final Data for 2017. *Natl Vital Stat Rep.* 68:9.

La Grutta, L., Toia, P., Maffei, E., Cademartiri, F., Lagalla, R., and Midiri, M. 2017. Infarct characterization using CT. *Cardiovasc Diagn Ther.* 7:171-188.

Levi, F., Lucchini, F., Negri, F. and La Vecchia, C. 2002. Trends in mortality from cardiovascular and cerebrovascular diseases in Europe and other areas of the world. *Heart*. 88:119-124.

Li, Y., Zhang, W., Wu, H., and Liu, G. 2014. Advanced Tracers in PET Imaging of Cardiovascular Disease. *Biomed Res Int.* 2014:504532. doi: 10.1155/2014/504532.

Lin, E. and Alessio, A. 2009. What are the basic concepts of temporal, contrast and spatial resolution in cardiac CT? *J Cardiovasc Comput Tomogr.* 3:403-408.

Livieratos, L. 2013. Basic Principles of SPECT and PET Imaging. In: *Radionuclide and Hybrid Bone Imaging,* pp. 345-359. Springer, New York.

Lu, H., and A. Daugherty. 2015. Recent Highlights of ATVB Atherosclerosis. *Arterioscler Thromb Vasc Biol.* 35:485-491.

Mankoff, D. A. 2007. A definition of molecular imaging. *J Nucl Med.* 28:18N, 21N.

Melcher, C. L. 2000. Scintillation Crystals for PET. *J Nuc Med.* 41:1051-1055.

Mikla, V. I.; Mikla V. V. 2014. Computed Tomography. In: *Medical Imaging Technology*, pp.23-38. Elsevier, Amsterdam.

Mikla, V. I.; Mikla V. V. 2014. Positron Emission Tomography. In: *Medical Imaging Technology*, pp. 53-64. Elsevier, Amsterdam.

Minicucci, M., Azevedo, P. S., Polegato, B. F., Paiva, S. A. R., and Zornoff, L. A. M. 2011. Heart Failure After Myocardial Infarction: Clinical Implications and Treatment. *Clin Cardiol.* 34:410-414.

Murray, C. J. L., D. Phil, and A. D. Lopez. 2013. Measuring the Global Burden of Disease. *N Engl J Med*. 369:448-457.

Napoli, C., D'Armiento, P. D., Mancini, F. P., Postiglione, A., Witztum, J. L., Palumbo, G., and Palinski, W. 1997. Fatty Streak Formation Occurs in Human Fetal Aortas and is Greatly Enhanced by Maternal Hypercholesterolemia. *J Clin Invest.* 100:2680-2690.

Naresh, N. K., Ben-Mordechai, T., Leor, J., Epstein, F. H. 2012. Molecular Imaging of Healing After Myocardial Infarction. *Curr Cardiovasc Imaging Rep.* 4:63-76.

Neves, P. O., Andrade, J., and Monção, H. 2017. Coronary artery calcium score: current status. *Radiol Bras.* 50:182-189.

Overdick, M. 2006. Detectors for X-Ray Imaging and Computed Tomography. In: *Advances in Healthcare Technology,* pp.49-64. Springer, the Netherlands.

Rafieian-Kopaei, M., Setorki, M., Doudi, M., Baradaran, A., and Nasri, H. 2014. Atherosclerosis: Process, Indicators, Risk Factors and New Hopes. *Int J Prev Med.* 5:927-946.

Rajiah, P., Desai, M. Y., Kwon, D., and Flamm, S. D. 2013. MR Imaging of Myocardial Infarction. *Radiographics.* 33:1383-1412.

Roger, V. L. 2007. Epidemiology of Myocardial Infarction. *Med Clin North Am.* 91:537-552.

Rominger, A., Saam, T., Vogl, E., Übleis, C., la Fougère, C., Förster, S., Haung, A., Cumming, P., Reiser, M. F., Nikolaou, K et al. 2010. In Vivo Imaging of Macrophage Activity in the Coronary Arteries Using ^{68}Ga-DOTATATE PET/CT: Correlation with Coronary Calcium Burden and Risk Factors. *J Nucl Med.* 51: 193-197.

Sergeev, M., Lazari, M., Morgia, F., Collins, J., Javed, M. R., Sergeeva, O., Jones, J., Phelps, M. E., Lee, J. T. et al. 2018. Performing radiosynthesis in microvolumes to maximize molar activity of tracers for positron emission tomography. *Commun Chem.* 1. doi: 10.1038/s42004-018-0009-z.

Shah, P. K. 2010. Screening Asymptomatic Subjects for Subclinical Atherosclerosis: Can We, Does It Matter, and Should We? *J Am Coll Cardiol.* 56:98-105.

Silvola, J. M. U., Laitinen, I., Sipliä, H. J., Laine, V. J. O., Leppänen, P., Ylä-Herttuala, S., Knuuti, J., and Roivainen, A. 2011. Uptake of ^{68}gallium in atherosclerotic plaques in LDLR$^{-/-}$ApoB$^{100/100}$ mice. *EJNMMI Res*. 1:14. doi: 10.1186/2191-219X-1-14.

Silvola, J. M. U., X. G. Li, J. Virta, P. Marjamäki, H. Liljenbäck, J. P. Hytönon, M. Tarkia, V. Saunavaara, S. Hurme, S. Palani et al. 2018. Aluminum fluoride-18 labeled folate

enables *in vivo* detection of atherosclerotic plaque inflammation by positron emission tomography. *Sci Rep*. 9720.

Spanoudaki, V. C., Levin, C. S. 2010. Photo-Detectors for Time of Flight Positron Emission Tomography (ToF-PET). *Sensors (Basel).* 10:10484-10505.

Ståhle, M., V. Kytö, M. Kiugel, H. Liljenbäck, O. Metsälä, X. Li, V. Oikonen, P. Saukko, P. Nuutila, J. Knuuti et al. 2018. Glucagon-like peptide-1 receptor expression after myocardial infarction: Imaging study using ^{68}Ga-NODAGA-exendin-4 positron emission tomography. *J. Nucl. Cardiol.* doi: 10.1007/s12350-018-01547-1

Studer, M., and C. F. Meares. 1992. Synthesis of Novel 1,4,7-Triazacyclononane-*N,N',N''*-triacetic Acid Derivatives Suitable for Protein Labeling. *Bioconjugate Chem.* 3:337-341.

Tarkin J. M., F.R. Joshi, N.R. Evans, M. M. Chowdhury, N. L. Figg, A. V. Shah, L. T. Starks, A. Martin-Garrido, R. Manavaki, E. Yu et al. 2017. Detection of Atherosclerotic Inflammation by ^{68}Ga-DOTATATE PET Compared to [^{18}F]FDG PET Imaging. *J Am Coll Cardiol*. 69:1774-1791.

Tarkin, J. M., Calcagno, C., Dweck, M. R., Evans, N. R., Chowdhury, M. M., Gopalan, D., Newby, D. E., Fayad, Z. A., Bennett, M. R., and Rudd, J. H. F. 2019. ^{68}Ga-DOTATATE PET Identifies Residual Myocardial Inflammation and Bone Marrow Activation After Myocardial Infarction. *J Am Coll Cardiol.* 73:2489-2491.

Thackeray, J. T., Bankstahl, J. P., Wang, Y., Korf-Klingebiel, M., Walte, A., Wittneben, A., Wollert, K. C., and Bengel, F. K. 2015. Targeting post-infarct inflammation by PET imaging: comparison of ^{68}Ga-citrate and ^{68}Ga-DOTATATE with ^{18}F-FDG in a mouse model. *Eur J Nucl Med Mol Imaging.* 42:317-327

Thygesen, K., Alpert, J. S., White, H. D., Jaffe, A. S., Apple, F. S., Galvani, M., Katus, H. A., Newby, K., Ravkilde, J., Chaitman, B. et al. 2007. Universal definition of myocardial infarction: Kristian Thygesen, Joseph S. Alpert and Harvey D. White on behalf of the Joint ESC/ACCF/AHA/WHF Task Force for the Redefinition of Myocardial Infarction. *Eur Heart J.* 28:2525-2538.

Van der Laan, A. M., M. Nahrendorf, and J. J. Piek. 2012. Healing and adverse remodeling after acute myocardial infarction: role of the cellular immune response. *Heart*. 98:1384-1390.

Velikyan, I. 2018. Prospective of ^{68}Ga Radionuclide Contribution to the Development of Imaging Agents for Infection and Inflammation. *Contrast Media Mol Imaging.* 2018:9713691.

Véniant, M. M., Zlot, C. H., Walzem, R. L., Pierotti, V., Driscoll, R., Dichek, D., Herz, J., and Young, S. G. 1998. Lipoprotein Clearance Mechanisms in LDL Receptor-Deficient "Apo-B48-only" and "Apo-B100-only" Mice. *Jour Clin Invest.* 102:1559-1568.

Virani, S. S., Alonso, A., Benjamin, E. J., Bittencourt, M. S., Callaway, C. W., Carson, A. P., Chamberlain, A. M., Chang, A. R., Cheng, S., Delling, F. N., et al. 2020. Heart Disease and Stroke Statistics—2020 Update: A Report From the American Heart Association. *Cir.* 141.

Warraich, H. J., Benson, C. C., Khosa, F., and Leeman, D. E. 2014. Diagnosis of acute myocardial infarction on computed tomography angiogram. *Circ*. 129:272-273.

Willemink, M. J. and Noël, P. B. The evolution of image reconstruction for CT—from filtered back projection to artificial intelligence. *Eur Radiol.* 29:2185-2195.

Yamamoto, L. G. 2013. Risks and Management of Radiation Exposure. *Pediatr Emer Care*. 29:1016-1029.